

# The magma and metal source of giant porphyry-type ore deposits, based on lead isotope microanalysis of individual fluid inclusions

**Journal Article****Author(s):**

Pettke, Thomas; Oberli, Felix; [Heinrich, Christoph A.](#) 

**Publication date:**

2010-08

**Permanent link:**

<https://doi.org/10.3929/ethz-b-000157728>

**Rights / license:**

[Creative Commons Attribution-NonCommercial-NoDerivatives 4.0 International](#)

**Originally published in:**

Earth and Planetary Science Letters 296(3-4), <https://doi.org/10.1016/j.epsl.2010.05.007>

1    **The magma and metal source of giant porphyry-type**  
2    **ore deposits, based on lead isotope microanalysis of**  
3    **individual fluid inclusions**

4

5    **Thomas Pettke<sup>a,b</sup>, Felix Oberli<sup>a</sup> and Christoph A. Heinrich<sup>a,c</sup>**

6    <sup>a</sup> ETH Zürich, Department of Earth Sciences, Institute of Geochemistry and Petrology,  
7    Clausiusstrasse 25, CH-8092 Zürich, Switzerland.

8    <sup>b</sup> University of Bern, Institute of Geological Sciences, Baltzerstrasse 1+3, CH-3012 Bern,  
9    Switzerland

10    <sup>c</sup> also at University of Zurich, Faculty of Mathematics and Natural Sciences, Zurich,  
11    Switzerland

12

13    corresponding author:

14    pettke@geo.unibe.ch

15    phone    ++41 31 631 5059

16

17    **Please cite as:**

18    **Pettke, T., Oberli, F., and Heinrich, C. A., 2010. The magma and metal**  
19    **source of giant porphyry-type ore deposits, based on lead isotope**  
20    **microanalysis of individual fluid inclusions. Earth and Planetary Science**  
21    **Letters 296, 267-277.**  
22    **DOI: 10.1016/j.epsl.2010.05.007**

## Abstract

The global supply of Mo and much of Cu and Au comes from porphyry-type ore deposits associated with hydrous magmas of broadly calc-alkaline composition, thought to be generated by contemporaneous subduction zone processes. Molybdenum is generally considered to be derived from the continental crust while Cu and Au are sourced in the mantle wedge above subducting slabs. Here we show that neither contemporaneous subduction nor derivation of Mo from crustal sources is required to explain the genesis of porphyry-Cu-Mo-Au deposits on Proterozoic lithosphere in the eastern Rocky Mountains.

Uniform Pb isotope ratios measured by LA-MC-ICP-MS in individual fluid inclusions from distinct Cu-Au and later Mo ore-forming stages at Bingham Canyon, USA, demonstrate a common metal source. Uranogenic Pb isotope ratios are particularly non-radiogenic ( $17.494 < {}^{206}\text{Pb}/{}^{204}\text{Pb} < 17.534$ ;  $15.553 < {}^{207}\text{Pb}/{}^{204}\text{Pb} < 15.588$ ) and plot to the left of the geochron and above the mantle Pb evolution line. In  ${}^{207}\text{Pb}/{}^{206}\text{Pb}$  vs.  ${}^{208}\text{Pb}/{}^{206}\text{Pb}$  space, the fluid Pb isotope data cluster at the non-radiogenic end of a mixing line described by >80 feldspar data from igneous rocks intimately associated with magmatic-hydrothermal ore formation, which extends to modern depleted mantle or upper crust. Forward Monte Carlo simulations require three events for the U-Th-Pb isotope evolution of the fluid: (1) Late Archean formation of enriched crust is followed by (2) preferential extraction of Pb from this aged crust into a subduction fluid characterized by drastically reduced U/Pb that metasomatized lithospheric mantle at ~ 1.8 Ga. This mantle reservoir then evolved to produce the retarded uranogenic Pb isotope signatures of the Bingham Canyon Cu-Mo-Au deposit in the Cenozoic (3).

Similarly retarded uranogenic Pb isotope data characterize the giant porphyry-Mo and Climax-type Mo deposits of Henderson, Questa, Butte, and SE Arizona that occur in Proterozoic sutures of the central and eastern Rocky Mountains. We propose that Cenozoic melting of subcontinental lithospheric mantle metasomatized by subduction fluids during early Proterozoic amalgamation of terranes to the Wyoming Craton provides the metal endowment and subduction flavour to the giant magmatic-hydrothermal Cu-Mo-Au ore deposits in western North America, which together constitute the world's major molybdenum ore province.

## Keywords:

47 Proterozoic subduction metasomatism,  
48 subcontinental lithospheric mantle,  
49 Post-collisional ore deposit,  
50 lead isotopes,  
51 laser ablation ICPMS

## 52 **1. Introduction**

53 Porphyry-type ore deposits form from hydrothermal fluid circulation in and around small  
54 intrusions atop large, intermediate to felsic, subvolcanic magma chambers that source the  
55 ore-forming fluid and most of the metals (e.g., Burnham, 1979; Dilles, 1987; Halter et al.,  
56 2002, 2005; Williams-Jones and Heinrich, 2005). Magma mixing, fractional crystallization and  
57 assimilation characterize these magmatic systems, sustained through repeated injection of  
58 basic mantle-derived magma providing heat and chemical components (Hildreth, 1981;  
59 Hattori and Keith, 2001; Maughan et al., 2002; Halter et al., 2005). Upper-crustal processes of  
60 ore formation are fairly well understood, but far less is known about the deep source  
61 characteristics of ore-forming magmas and their metals. This is partly due to hydrothermal  
62 alteration in subvolcanic intrusions hosting the ore deposits, which erases much of the earlier  
63 bulk geochemical and isotopic record. The debate is therefore alive, whether specific magma  
64 sources are required to form economically significant deposits of Cu, Mo and Au, but also of  
65 W, Sn, and platinum-group elements including Re. Empirical evidence for lithosphere-scale  
66 source control includes the observation that some regions of the Earth seem particularly well  
67 endowed with certain types of ore deposits. Four of the world's six largest molybdenum  
68 deposits (Climax, Henderson, Butte, and Bingham Canyon) occur in the western USA within  
69 less than 1% of the Earth's land surface (Singer et al., 2005). If lithosphere-scale source  
70 characteristics are essential for such extraordinary metal accumulation, the potential of finding  
71 new ore resources of the same type would be largely limited to such provinces. Alternatively,  
72 if fluid processes in magmatic-hydrothermal systems in the shallow crust alone would account  
73 for the formation of these economic geochemical anomalies, any area with a suitable  
74 magmatic-hydrothermal architecture could become a target for exploration.

Fluid evolution and ore mineral precipitation in hydrothermal systems are recorded by multiple generations of fluid inclusion assemblages and mineral inclusions, and their trapping sequence can be established through careful thin-section petrography. At concentrations of several thousand  $\mu\text{g Pb per g of fluid}$  (e.g., Landtwing et al., 2005; Seo et al., 2009; Klemm et al., 2008), the hydrothermal fluid is by far the most Pb enriched phase conserved in the high-temperature magmatic-hydrothermal ores; co-existing minerals contain traces of Pb only. Compositional modification of fluid inclusions after their entrapment in non-reactive quartz is unlikely or can be recognized by petrography or microthermometry, whereas trace amounts of Pb in porphyry-stage minerals (feldspars, Cu-Fe-sulphides) are easily modified by later, cooler fluids that commonly deposit galena (PbS) from a potentially different lead source. Direct analysis of Pb-rich high-temperature fluids therefore provides hitherto unavailable, controlled access to the most pristine Pb isotopic signatures of magmatic-hydrothermal ore-forming systems.

As a new and direct tracer of magmatic fluid source, we report the first in-situ measured Pb isotopic data of individual fluid inclusions from Mo and Cu-Au mineralized veins and magmatic feldspar phenocrysts for the porphyry-Cu-Au-Mo deposit at Bingham Canyon, Utah (Fig. 1), one of the world's largest and best-studied porphyry-type volcano-plutonic systems (e.g., Stacey et al., 1968; Waite et al., 1997; Maughan et al., 2002; Redmond et al., 2004; Redmond and Inaudi, 2010; Landtwing et al., 2005, 2010). We use radiogenic isotope systematics, because these retain a memory of processes which predate the formation of the fluid-generating magmas. Lead isotope systematics are particularly powerful because three radioactive decay chains produce distinct Pb isotopes ( $^{238}\text{U} \rightarrow ^{206}\text{Pb}$ ,  $^{235}\text{U} \rightarrow ^{207}\text{Pb}$  and  $^{232}\text{Th} \rightarrow ^{208}\text{Pb}$ ). Besides source fingerprinting, Pb isotopes also provide time-integrated information on Pb/U/Th ratios in the melt source, elements that are particularly sensitive to fractionation during fluid-assisted processes in the mantle and crust. Monte Carlo simulations are used to evaluate radiogenic Pb growth scenarios able to reproduce our measured Pb isotope signatures of the ore-forming fluid. Consistent with independent geological and geophysical constraints, we propose that ore-forming magmas and their metal endowment, including notably those sourcing porphyry-type Cu-Mo, Cu-Mo-Au and even large Climax-type Mo deposits in the eastern Rocky Mountains of the USA are derived from anciently

metasomatized subcontinental lithospheric mantle. Contrary to current views, significant input from evolved lower crustal sources, especially for Mo, appears unlikely.

## **2. Bingham geology and sample characterization**

The giant Cu-Au-Mo deposit at Bingham Canyon formed in the late Eocene as part of a now partly eroded volcano-plutonic complex composed of calc-alkaline to shoshonitic and subordinate alkaline magmatic rocks (e.g., Maughan et al., 2002; Waite et al., 1997; Redmond and Einaudi, 2010). Hosted by a sequence of shallow monzonitic intrusions, it is situated in the Oquirrh Mountains in the easternmost part of the Basin and Range province. The Oquirrh mountains sit on the western projection of the Uinta axis, a Late Proterozoic basin extending along an even older continental suture (Presnell, 1997). To the east follows the Cheyenne Belt, which delineates the suture between Archean crust to the north (the Wyoming Province) and juvenile, accretionary, arc-like, paleo-Proterozoic terranes in the south (Dueker et al., 2001; Karlstrom et al., 2004; Mueller and Frost, 2006; Fig. 1).

In the Bingham Canyon deposit, alternating dyke intrusion and veining phases document an intimate relationship between magmatic and hydrothermal activity (Fig. 2). Cross-cutting relationships demonstrate that all Cu ± Au veins are older than a distinct last generation of veins containing most of the molybdenite (MoS<sub>2</sub>), which formed after the last stage of dyke intrusion (Redmond et al., 2004; Redmond and Inaudi, 2010).

Samples of quartz - chalcopyrite (Cu-Au stage) and quartz - molybdenite (Mo stage) veins contain numerous pseudosecondary fluid inclusion assemblages, which can be petrographically related to distinct phases of Cu-sulphide and molybdenite mineralization (Fig. 2). The trapping history of the fluid inclusions plus extensive microthermometric and compositional data are reported in Landtwing et al. (2005, 2010). Both pulses of ore formation occurred between 425 - 350 °C from two-phase aqueous fluids (vapour and brine), which formed by phase separation from a single-phase magmatic-hydrothermal fluid of ~7 wt-% NaCl<sub>equivalent</sub> bulk salinity.

Late Eocene shallow intrusive rocks hosting the Bingham porphyry-type Cu-Au±Mo deposit are almost pervasively altered, with the exception of relicts of large magmatic feldspar phenocrysts or xenocrysts. In-situ Pb isotope analyses were thus carried out on K-feldspar and plagioclase

from Quartz-Monzonite Porphyry (QMP), Biotite Porphyry (BP) and Quartz Latite Porphyry (QLP), three intrusions that, from old to young, bracket the hydrothermal Cu±Au input into the Bingham Canyon deposit (Waite et al., 1997). These late Eocene - early Oligocene magmas intruded Paleozoic quartzite and limestone. Co-existing plagioclase and K-feldspar were also analyzed in order to test for Pb isotope disequilibrium between different minerals in the same rock. One rock sample (D404-1676) was also tested for the effects of potassic alteration of K-feldspar on Pb isotope systematics.

Melanephelinite and shoshonite lavas of the less-altered volcanic section of mafic and variably alkaline magmas in Rose Canyon, some 9 km to the SSE of the Bingham Canyon mine, have been interpreted to be directly related to the ore-forming magmas (Maughan et al., 2002). Four bulk rock samples were thus also analyzed for Pb isotope ratios.

### 3. Analytical techniques

For in-situ Pb isotope analysis we use a new method of laser-ablation multiple-collector inductively-coupled-plasma mass-spectrometry (LA-MC-ICP-MS) developed at ETH Zurich (Pettke et al., 2008; electronic appendix ES 1). A Geolas ArF excimer laser system (Lambda Physik, Germany; Günther et al., 1998) is coupled to two different MC-ICP-MS instruments (Nu Instruments, Wrexham, UK). The pulsed laser beam opens and liberates the entire contents of individual inclusions in a controlled manner, and the fast transient Pb isotopic signals are simultaneously recorded on Faraday detectors in static mode. Mass bias correlation parameters between measured  $^{205}\text{Ti}/^{203}\text{Ti}$  and Pb isotope ratios are established by measurements on NIST SRM 610 glass and then applied for within-run correction of the fluid inclusion analyses employing aspirated, desolvated Ti (Baxter et al., 2006). Isobaric interference by Hg on mass 204 is subtracted based on measured  $^{202}\text{Hg}$  intensities; other interferences were insignificant at the analytical precision obtained, even for SRM 610 glass, a trace element doped (nominally 500 µg/g) standard reference material. The analytical procedure has been successfully tested on synthetic Na-K-Pb-Cl fluid inclusions of known Pb isotopic composition (SRM 981), yielding accurate ratios for individual inclusions containing as little as 0.01 ng total Pb. The external precision achieved on our synthetic fluid inclusion analyses converges to ± 0.08% (2 s.d.) for  $^{208}\text{Pb}/^{206}\text{Pb}$  and  $^{207}\text{Pb}/^{206}\text{Pb}$  and to ± 0.4 % for Pb

isotope ratios containing mass 204. Magmatic feldspar phenocrysts and xenocrysts were analyzed with the same routine.

The same feldspar crystals were analyzed for their major and trace element compositions, using a GeolasPro laser system combined with a Perkin Elmer Elan DRC-e ICP-MS instrument at the University of Bern (see Pettke, 2008, for instrumental details and optimization strategies). Data quantification was based on SRM 612 for external calibration, and internal standardization was done by summation of all major element oxides to 100 wt-%. The accuracy of the data is routinely better than  $\pm 3$  % (2 s.d.).

Five bulk rock Pb isotopic analyses were also performed. Rocks were crushed and then powdered in agate mills. 100 mg aliquots of rock powder were digested in a mixture of 9:1 HF:HNO<sub>3</sub> at 180 °C in Savillex screwtop beakers. Lead was extracted from the samples employing mixed HNO<sub>3</sub>-HBr ion exchange procedures (Galer, 1986). Measurements were done on a Nu Plasma MC-ICP-MS at the University of Bern in static mode, using Faraday cups and employing TI addition for within-run correction of mass bias. Measurements on SRM 981 performed during the same session were identical to the reference values.

#### 4. Results

24 individual fluid inclusions from 8 assemblages in 5 samples were investigated in two analytical sessions (Table 1). The precise results (Fig. 3) document identical Pb isotopic signatures for the successive (Fig. 2) Cu-Au *and* Mo ore stages at Bingham Canyon. The Pb isotopic signatures are conspicuously non-radiogenic, with averages for individual fluid inclusion assemblages restricted to  $17.494 < {}^{206}\text{Pb}/{}^{204}\text{Pb} < 17.534$ ,  $15.553 < {}^{207}\text{Pb}/{}^{204}\text{Pb} < 15.588$ ,  $38.22 < {}^{208}\text{Pb}/{}^{204}\text{Pb} < 38.31$ ,  $0.88805 < {}^{207}\text{Pb}/{}^{206}\text{Pb} < 0.88955$ ,  $2.1803 < {}^{208}\text{Pb}/{}^{206}\text{Pb} < 2.1853$ . Such a non-radiogenic signature is rare for Phanerozoic rocks and has never been reported for classical subduction-related calcalkaline magmas, with or without associated porphyry-type ore deposits. Data on element concentrations of Mo, Cu, Au, Pb, U and Th are also reported in Table 1. For Bingham ore fluids, measured U/Pb ratios are  $\sim 0.001$  and Th/Pb ratios are  $\ll 0.001$ ; hence, correction for in-situ grown radiogenic Pb since fluid inclusion formation at ca. 38 Ma (Parry et al., 2001) is insignificant. We thus report measured Pb isotope ratios.



The fluid inclusion results lie at the non-radiogenic end of a linear trend in  $^{207}\text{Pb}/^{206}\text{Pb}$  vs.  $^{208}\text{Pb}/^{206}\text{Pb}$  space defined by ~80 in-situ analyses on feldspar phenocrysts and xenocrysts from the associated intrusions (Fig. 4; Electronic Supplementary Table ES2). This linear trend extends towards more radiogenic values of present-day depleted mantle. Some K-feldspar phenocrysts host melt and fluid inclusions. Inclusion-poor and inclusion-rich analyses randomly align along the same Pb isotopic trend; the one analysis on a sample devoid of inclusions lies in the central part of the trend (Fig. 5A). Lead isotope systematics in co-existing K-feldspar and plagioclase often show Pb isotope disequilibrium within the same rock (Fig. 5B), their data conforming to the same trend, however.

Compositionally, the feldspars are strikingly uniform (Table ES2). Most importantly, all feldspar analyses have U/Pb and Th/Pb abundance ratios smaller than 0.0003 and 0.0002, respectively, thus requiring no correction for in-situ grown Pb since 38 Ma. Anorthite contents in plagioclase vary little across the successive intrusions, from An<sub>22</sub> to An<sub>25</sub>. K-feldspar Na<sub>2</sub>O/K<sub>2</sub>O ratios are variable. Inclusion-free K-feldspar (e.g., sample 4890-2080) has Na<sub>2</sub>O/K<sub>2</sub>O up to 0.28, while inclusion-rich feldspar domains from hydrothermally overprinted sample D404-1676 are characterized by Na<sub>2</sub>O/K<sub>2</sub>O ~0.14, consistent with ore-related potassic alteration. Contents of Ba are 1 wt-% on average, in line with the conspicuously high Ba contents of the bulk rocks (Maughan et al., 2002).

Bulk rock Pb isotope data for the melanephelinite and shoshonite rock suites, which occur peripherally to the Bingham Canyon mine and were considered to be co-sanguineous with the ore-forming magma (Waite et al., 1997, Maughan et al., 2002), do not plot on the Bingham Pb isotope trend (Fig. 4) but are enriched in  $^{208}\text{Pb}$  relative to  $^{207}\text{Pb}$ . The melanephelinite samples show the most radiogenic Pb isotope compositions measured on Bingham magmas, interpreted to reflect the most significant addition of present-day common mantle Pb, this being in tune with their largest content of compatible elements. However, the Pb isotopic composition of the propylitically altered pre-mineralization Equigranular Monzonite sample from the Bingham Canyon pit plots on the mixing trend defined by the in-situ feldspar and fluid inclusion analyses.

## 5. Discussion: Source of Bingham ore fluids

The fluid Pb isotope signatures for the chemically distinct and temporally successive Cu-Au and Mo mineralization stages of the Bingham Canyon deposit are identical, implying a common metal source. The ore fluids occupy the non-radiogenic end of a dominantly binary mixing array populated by feldspar phenocryst data from the ore-related porphyry intrusions (Figs. 4, 5). These subvolcanic intrusions are too small to be the source of the ore fluids, indicating that the ore fluids and the subvolcanic intrusions originate from a common, much larger but only partially homogenized magma reservoir (cf. Halter et al., 2005). The more radiogenic lead isotope component of the feldspar phenocryst mixing array may be of mid- to upper crustal derivation (cf. Stacey et al., 1968) or may represent addition of a common mantle component. The non-radiogenic mixing component dominating in the ore fluids thus represents a deep endmember component and probably relates to the magma source that also contributed the ore metals. The origin of this deep and retarded uranogenic lead component plotting to the left of the geochron (Fig. 6A) is the focus of the following discussion.

### **5.1 A lower crustal magma and metal source?**

The classic view on Cretaceous to Tertiary evolved magmatism in Precambrian crustal domains of the Rocky Mountains, including the Bingham – Uinta district, interprets the dominant parental melt to be derived from evolved lower continental crust assembled during the Proterozoic (e.g., Stacey et al., 1968; Zartman, 1974; Farmer and De Paolo, 1983, 1984). Arguments for this lower-crustal melt source are based on combined radiogenic isotope systematics (variably negative present-day  $\epsilon_{\text{Nd}}$ , moderately radiogenic Sr, and non-radiogenic Pb isotope ratios) and the often peraluminous character of the most evolved magmas.

Figure 6 compares xenolith Pb isotope data for lower crust and lithospheric mantle below western North America with the Bingham data. Lower crustal xenolith data scatter strongly and plot above the MORB-source mantle evolution line, for the Archean Wyoming Craton at variably low  $^{206}\text{Pb}/^{204}\text{Pb}$ , and for Proterozoic crust at variably higher  $^{206}\text{Pb}/^{204}\text{Pb}$ . Xenoliths of metasomatized subcontinental lithospheric mantle from the Wyoming Craton and the adjacent Great Falls Tectonic Zone tend to have  $^{206}\text{Pb}/^{204}\text{Pb}$  ratios intermediate to these groups and cluster around the Bingham data, with slightly elevated  $^{207}\text{Pb}/^{204}\text{Pb}$  and less radiogenic

$^{206}\text{Pb}/^{204}\text{Pb}$  compared to Proterozoic crustal xenoliths. Galena and feldspar data from the Bingham - Oquirrh region plot at high  $^{207}\text{Pb}/^{204}\text{Pb}$  for a given  $^{206}\text{Pb}/^{204}\text{Pb}$ , identified by Stacey et al. (1968) as mixing between subordinate upper crustal radiogenic Pb and a more remote Pb source assumed to be ancient lower crust. While the scatter in the feldspar  $^{206}\text{Pb}/^{204}\text{Pb}$  data might be due to upper-crustal contamination or represent subordinate contribution of modern mantle Pb (as indicated by the extension of the feldspar data towards Aleutian arc lava signatures), the source of the endmember component dominating the fluid data remains ambiguous. Lead, Nd and Sr isotope systematics alone do not allow a clear distinction between a lower crustal and a modified lithospheric mantle source of the parental magmas. As an alternative to lower-crustal melt generation, other workers have favoured a metasomatized lithospheric mantle source for mafic magma components with comparable radiogenic isotope systematics, occurring in Proterozoic crustal domains characterized by lithospheric thinning (e.g., Kempton et al., 1991; Harry and Leeman, 1995; Hawkesworth et al., 1995; Johnson et al., 1990; Johnson, 1991; Hart et al., 1997).

## **5.2 An ancient lithospheric mantle magma and metal source for Bingham Canyon**

In the following section, we show that the ore-fluid endpoint can be explained by a quantitative U-Th-Pb evolution model, in which the parental magma is derived by melting a subcontinental lithospheric mantle that had been metasomatized by subduction fluids about 1.8 billion years ago. The model reproduces the present-day Pb isotope ratios measured in the ore fluids, while satisfying independent geochemical and geodynamic boundary conditions. Two long-lasting evolution stages bounded by three events are required by the uranogenic Pb isotope signatures to have affected the source region of the Bingham magmas, as indicated schematically in Figure 7 and tested with Monte Carlo simulations (Table 2). Thorogenic Pb systematics contribute complementary information only, but are consistent with the model. One-stage evolution models cannot satisfy uranogenic Pb isotope systematics and are therefore rejected. Variations of  $\pm 0.2$  Ga in the timing of events 1 and 2 are easily tolerated in our preferred model, variations that exceed those permitted by the known geological evolution of the region. Figure 8 depicts our preferred Pb evolution model, which leads to the conspicuously non-radiogenic Pb isotopic composition of the ore-forming fluid that lies to the left of the geochron and above the MORB source mantle evolution line

(Kramers and Tolstikhin, 1997), in  $^{207}\text{Pb}/^{204}\text{Pb}$  and  $^{208}\text{Pb}/^{204}\text{Pb}$  vs.  $^{206}\text{Pb}/^{204}\text{Pb}$  representation, together with the three major events marked by solid stars.

**Event 1:** Late Archean juvenile crust formation is widespread in western North America (Carlson and Irving, 1994; Chamberlain et al., 2003; Souders and Frost, 2006; Frost et al., 2006a). This was the first essential event, leading to elevated  $\mu$  values ( $^{238}\text{U}/^{204}\text{Pb}$ ) because of the higher incompatibility of U relative to Pb during shallow partial mantle melting. Melt extraction from a MORB-source mantle (Kramers and Tolstikhin, 1997) during the late Archean (Table 2, simulation 1) would necessitate very high  $\mu_1$  values ( $>14.0$ ) for newly formed crust (stage 1), too high to be compatible with significant fractions of mantle melting. U-Pb fractionation factors between such a MORB source mantle and its melt products as required by the model would become lower and thus more plausible for significantly older separation ages (e.g., 3.2 Ga; simulation 2), but there is no independent indication for significant mid-Archean crust formation in the southern Wyoming Province (e.g., Chamberlain et al., 2003; Frost et al., 2006a). Consequently, melt extraction from an already evolved Pb isotope reservoir is indicated, i.e., a high- $\mu$  late Archean mantle, modified perhaps by recycling of older crustal materials. Our simulation 5 (Table 2) returns a plausible  $\mu$  value of 8.5 for this mantle reservoir, consistent with the enriched mantle reservoir proposed for the late Archean Wyoming Province ( $8.5 > \mu > 8.65$ ; Frost et al., 2006b; Mueller and Frost, 2006). The late Archean crust produced by Event 1 subsequently evolved in isolation for about 1 Ga (stage 1 from 2.8 - 1.8 Ga; Fig. 8), resulting in time-integrated Pb isotope signatures that plot well above the MORB-source mantle of Kramers and Tolstikhin (1997) or a primitive mantle evolution line in  $^{207}\text{Pb}/^{204}\text{Pb}$  vs.  $^{206}\text{Pb}/^{204}\text{Pb}$  space.

**Event 2:** Subduction and accretion of arc terranes to the Wyoming Craton along its southern, western and north-western margins assembled Laurentia around 1.8 Ga (e.g., Chamberlain, 1998; Mueller et al., 2002; Karlstrom et al., 2004; Foster et al., 2006; Mueller and Frost, 2006). The Cheyenne Belt (Fig. 1) marks the suture between Archean crust to the North and juvenile 1.8-1.7 Ga Proterozoic island arc crust. A north-dipping, high velocity mantle anomaly beneath the southern rim of the Wyoming Craton is still visible today, most likely representing an ancient slab fragment subducted at  $\sim 1.8$  Ga (Dueker et al., 2001; Karlstrom et al., 2004). We propose that this Event 2 metasomatized a depleted mantle wedge above the northward

subducted Cheyenne slab, by fluids that devolatilized from late Archean crustal material produced in Event 1 (Fig. 7). Slab fluids are characterized by enrichment in light rare earth elements (LREE) and large ion lithophile elements (LILE), most importantly K, Pb, Rb, Ba and Sr (e.g., Kessel et al., 2005). The resulting lowered Sm/Nd and moderately elevated Rb/Sr ratios are consistent with the present-day negative  $\epsilon_{Nd}$  and moderately radiogenic Sr isotopic ratios measured in Bingham magmas (e.g., Maughan et al., 2002, Waite et al., 1997). Most importantly, this subduction metasomatism led to drastically reduced  $\mu$  values in the mantle beneath Bingham (simulations 1 - 5 in Table 2), as the enrichment of Pb >> U is diagnostic for an aqueous fluid component released during devolatilization of crust at cool, sub-solidus conditions and shallower than about 150 km (Kessel et al., 2005). Mass balance modelling demonstrates that addition of aqueous slab fluids to depleted mantle will dominate the incompatible element inventory of the metasomatized mantle product and thus its U-Th-Pb system. Consequently, we interpret the elevated  $^{207}\text{Pb}$  signature as compared to MORB-source mantle Pb isotopic composition as a signature of subducted late Archean crust, transferred to the overlying mantle wedge at 1.8 Ga. Phlogopite-bearing and partially veined (veining dated at ~1.8 Ga) dunite and harzburgite xenoliths from Eocene minette dikes intruded within and along the NW margin of the Wyoming craton in the Great Falls Tectonic Zone (Fig. 1; Carlson and Irving, 1994) may represent samples of such a metasomatized lithospheric mantle analogue. After terrane amalgamation in Event 2, the metasomatized material evolved in isolation as subcontinental lithospheric mantle for ~1.7 billion years (stage 2; Fig. 8), until the onset of Cenozoic magmatic activity.

**Event 3:** Cenozoic magmatism at Bingham Canyon probably involved dominant melting of this ancient metasomatized mantle plus a smaller contribution from ordinary (depleted) mantle, to generate the binary lead isotope mixing trend recorded by the igneous feldspars and the ore fluids (Fig. 4). It has been tentatively argued that the calcalkaline to shoshonitic subduction flavour of late Eocene Bingham magmas may be related low-angle subduction of the Farallon Plate beneath western North America (Maughan et al., 2002; Waite et al., 1997). However, the lead isotopes show little, if any, contribution of Pb from modern oceanic lithosphere, and the subduction front was >500 km to the west of Bingham, farther away than what can be reconciled with common subduction zone geometries and subsequent basin-

and-range extension. Moreover, preservation of a Proterozoic lithospheric keel >200 km thick beneath the eastern Rocky Mountains (Karlstrom et al., 2004) is inconsistent with a model of low-angle subduction of the Farallon plate reaching as far east as Bingham. We therefore propose that incipient extensional tectonics during late Eocene triggered partial melting of subcontinental lithospheric mantle domains below the Bingham area, and that the modern magmas and fluids acquired their subduction signature from an event that occurred some 1.7 Ga earlier (Fig. 7). Metasomatized mantle rocks are expected to melt selectively at lower temperature than enclosing depleted peridotite (Leeman and Harry, 1993). High degrees of melting of metasomatized mantle rocks (e.g., phlogopite + orthopyroxene + clinopyroxene ± amphibole - veined harzburgite as sampled in xenoliths from the Great Falls Tectonic Zone; Carlson and Irving, 1994; Downes et al., 2004) can produce voluminous mafic magmas of mildly alkaline character (Pilet et al., 2008) rich in incompatible elements, consistent with Pb isotope data as well as the arc-like trace element signature and the conspicuous Ba enrichment that characterize Bingham magmas (Maughan et al., 2002, Waite et al., 1997). It is conceivable that substantial enrichments in highly refractory elements such as Ni, Cr and Mg (Maughan et al., 2002, Waite et al., 1997) and the subordinate radiogenic Pb component originated from interaction of the lithospheric melts with non-metasomatized portions of depleted subcontinental lithospheric mantle. Our fluid Pb isotope results clearly demonstrate, that modern mantle derived Pb is, at most, a minor component in these magmas, consistent with the Nd-Sr-Pb systematics of the previous studies.

## **6. Ancient, metasomatized mantle: key to a global ore province**

Four of the six largest molybdenum deposits in the world (Henderson, Climax, Bingham Canyon, Butte) and several other world-class Mo ± Cu deposits are located in the western USA. We propose that the geodynamic and geochemical source model developed for Bingham Canyon also applies to these other giant Mo-rich ore deposits, and that such an extended lithospheric pre-history may be a defining hallmark and essential metallogenic component of the premier global molybdenum province.

All four giant deposits and several other Mo-rich ore districts in this province are located along Proterozoic lithospheric boundaries (Fig. 1). The ancient suture zones are delineated by

velocity contrasts in mantle tomography images resulting from compositional heterogeneities (Dueker et al., 2001; Karlstrom et al., 2004). Climax and Henderson lie in the Colorado Mineral Belt, interpreted to follow a NE striking Proterozoic arc-arc suture. The Mo-deposit at Questa, New Mexico, lies on the eastern flank of the Rio Grande Rift (Johnson et al., 1990), near the Jemez suture zone believed to represent the reactivated boundary between the 1.8-1.7 Ga Yavapai and Mazatzal Provinces. Near the SW end of this lineament, in the southern Eastern Transition Zone of the Basin and Range province (e.g., Kempton et al., 1991), Mo-rich Cu porphyries define the northern part of the SE Arizona district (SEAZ in Fig. 8). Finally, the giant Cu-Mo deposit at Butte, Montana (Doe et al., 1968), occurs at the southwest end of the Great Falls Tectonic Zone, a Proterozoic collisional suture between two Archean terranes (e.g., Mueller et al., 2002). These Mo-rich ore deposits occur in different crustal domains, but they all are located on or near Proterozoic crustal boundaries atop volatile-rich lithospheric mantle (e.g., Carlson and Irving, 1994; Downes et al., 2004; Karlstrom et al., 2004). Ore-forming Cenozoic magmatism occurred during early stages of tectonic perturbation (extension and/or asthenospheric upwelling) of these ancient lithospheric structures, with little or no temporal or spatial relationship to modern subduction.

All of these Mo-rich deposits and the associated magmas are characterized by retarded uranogenic Pb isotope signatures (Fig. 8). In any one magmatic-hydrothermal ore district, the ore minerals from the largest deposits and their most intimately associated igneous rocks show the most extreme uranogenic Pb isotope retardation compared to smaller deposits and less-directly ore-related magmas (Stacey et al., 1968; Doe et al., 1968; Bouse et al., 1999; Johnson et al., 1990; Stein and Hannah, 1985). Molybdenum endowment therefore seems to be correlated with the contribution of this retarded source component. The origin of this component has been suggested to be the lower crust, mainly because the molybdenum-only porphyries (Climax, Henderson, Questa) are all associated with highly silicic and partly peraluminous intrusions and variably non-radiogenic Nd and moderately radiogenic Sr isotope signatures (e.g., Farmer and DePaolo, 1984). However, several lines of evidence suggest that metasomatized subcontinental lithospheric mantle is at least a permissive alternative source, as previously suggested by Kempton et al. (1991), Johnson (1991) and Hawkesworth et al. (1995). All of the mineralized igneous complexes include at least minor mafic (~basaltic)

components (e.g., Johnson et al., 1990; Waite et al., 1997). Lower-crustal xenoliths in SE Arizona have distinctly more radiogenic  $^{206}\text{Pb}/^{204}\text{Pb}$  (Esperanca et al., 1988; Kempton et al., 1990) than the Mo-rich porphyries in this district (Bouse et al., 1999). Peraluminous granite magmas do not necessarily require sediment assimilation; they can also be generated by fractional crystallization of typical mantle-wedge melts of picrobasaltic composition (Muntener and Ulmer, 2006). The volume of basaltic melt required to generate progressively Mo-enriched felsic magmas (e.g., Carten et al., 1993) is consistent with partial melting of metasomatized subcontinental lithospheric mantle during early stages of extension, as discussed by Harry and Leeman (1995) for the Proterozoic Rocky Mountains domain. The isotopic composition of sulphur in giant molybdenum deposits is also consistent with fractionation of the associated rhyolitic magmas from mantle melts (Henderson, Questa:  $+1 < \delta^{34}\text{S} < 5.3 \text{ ‰}$ ; Stein and Hannah, 1985).

We propose that magmas originating from a metasomatized subcontinental lithospheric mantle are the decisive ingredient for the formation of giant Mo-rich porphyry deposits and this unique molybdenum ore province. Parental melt compositions were probably similar to basalts from the Eastern Transition Zone, characterized by high LIL/HFS element ratios and retarded uranogenic Pb signatures of an age of ca. 1.8 Ga (Kempton et al., 1991). Mafic magmatism commonly occurred late in the evolution of mineralized complexes (e.g., Maughan et al., 2002; Johnson et al., 1990), inconsistent with progressive melting of felsic crust. Sustained mantle magma input (e.g., Harry and Leeman, 1995; Hildreth and Moorbath, 1988) allows for protracted fractional crystallization promoting enrichment of the incompatible ore metals in the residual melt. Assimilation of lower crust lithologies, possibly indicated by more radiogenic  $^{208}\text{Pb}/^{204}\text{Pb}$  and less retarded  $^{206}\text{Pb}/^{204}\text{Pb}$  (Fig. 6), can be an ancillary consequence of long-lived magmatic systems (e.g., Hildreth and Moorbath, 1988), rather than a prerequisite to province-scale molybdenum enrichment as commonly inferred (e.g., Farmer and DePaolo, 1984; Bouse et al., 1999).

Our genetic model for Mo-rich porphyry deposits may also apply to the Gangdese belt in the Tibetan orogen. Here, world-class porphyry Cu-Mo deposits formed from high-K calcalkaline magmatism some 50 million years after arc magmatism (Hou and Cook, 2009). These systems are characterized by mantle-like  $\delta^{34}\text{S}$  but less radiogenic Nd, slightly more



radiogenic Sr, and enriched  $^{207}\text{Pb}/^{204}\text{Pb}$  ratios compared to present-day mantle (Qu et al., 2007), but lack the retarded uranogenic Pb isotope ratios due to the short time span between mantle metasomatism and melt extraction.

Lithospheric mantle domains enriched by ancient subduction metasomatism occur down to at least 200 km (e.g., Scambelluri et al., 2008) and may be a world-wide factor determining the distribution of major metal provinces and giant ore deposits. Based on global xenolith geochemistry and geophysical data, Griffin et al. (2009) concluded that the roots of most Proterozoic shields consist of refertilized Archean lithospheric mantle that has escaped reintegration into the convecting mantle, because strongly depleted but subsequently subduction-metasomatized mantle rocks are buoyant (cf. Carlson and Irving, 1994). The cause for selective mantle enrichment in Mo, but possibly also in S, Cu and Au is not clear. It could relate to the redox evolution of the latest Archean to early Proterozoic hydrosphere, which favoured the enrichment of chalcophile metals and gold in predominantly reduced deep-sea shales (e.g., Holland, 2005), prior to their subduction in a period of intensive continental (re)construction during the paleo-Proterozoic. Irrespective of the mechanism of this ancient mantle source enrichment, our results endorse modern approaches to global mineral exploration and resource assessment, which place increasing weight on mapping the chemical and thermal prehistory of large-scale lithospheric mantle domains, and on identifying their boundaries by geophysical methods and mantle xenolith data (Begg et al., 2009).

## Acknowledgments

We thank Jeff Keith for providing the melanephelinite and shoshonite samples, Bernard Bourdon and Jan Kramers for discussions on an early version of this manuscript, Andreas Audétat for the preparation of synthetic fluid inclusions and discussions on Mo ore deposits, and Rio Tinto for permission to publish this work. Two anonymous reviews are very much acknowledged, and we are grateful for the very thoughtful suggestions of Rick Carlson on how to revise our manuscript. Supported by the Swiss National Science Foundation grants PP002--106569 (TP) and 200020-107955 (CAH).

## References

457 Baxter, D.C., Rodushkin, I., Engstrom, E., Malinovsky, D., 2006. Revised exponential model  
 458 for mass bias correction using an internal standard for isotope abundance ratio  
 459 measurements by multi-collector inductively coupled plasma mass spectrometry. *J. Anal.*  
 460 *Atom. Spectrom.* 21, 427-430.

461 Begg, G.C., Griffin, W.L., Natapov, L.M., O'Reilly, S.P., Grand, S.P., O'Neill, C.J., Hronsky, Y.,  
 462 Djomani, P., Swain, C.S., Deen, T., Bowden, P., 2009. The lithospheric architecture of  
 463 Africa: Seismic tomography, mantle petrology, and tectonic evolution. *Geosphere* 5, 23-50.

464 Bolhar, R., Kamber, B.S., Collerson, K.D., 2007. U-Th-Pb fractionation in Archaean lower  
 465 continental crust: Implications for terrestrial Pb isotope systematics. *Earth Planet. Sci. Lett.*  
 466 254, 127-145.

467 Bouse, R.M., Ruiz, J., Titley, S.R., Tosdal, R.M., Wooden, J.L., 1999. Lead isotope  
 468 compositions of Late Cretaceous and early Tertiary igneous rocks and sulfide minerals in  
 469 Arizona: Implications for the sources of plutons and metals in porphyry copper deposits.  
 470 *Econ. Geol.* 94, 211-244.

471 Burnham, C.W., 1979. Magmas and hydrothermal fluids. In Barnes, H.L. (Ed.), *Geochemistry*  
 472 *of Hydrothermal Ore Deposits*, 2<sup>nd</sup> edition, Wiley, New York, 71-136.

473 Carlson, R.W., Irving, A.J., 1994. Depletion and enrichment history of subcontinental  
 474 lithospheric mantle - An Os, Sr, Nd and Pb isotopic study of ultramafic xenoliths from the  
 475 northwestern Wyoming Craton. *Earth Planet. Sci. Lett.* 126, 457-472.

476 Carlson, R.W., Irving, A.J., Schulze, D.J., Hearn, B.C., 2004. Timing of Precambrian melt  
 477 depletion and Phanerozoic refertilization events in the lithospheric mantle of the Wyoming  
 478 Craton and adjacent Central Plains Orogen. *Lithos* 77, 453-472.

479 Carten, R.B., White, W.H., Stein, H.J., 1993. High-grade granite-related molybdenum  
 480 systems: Classification and origin. In Kirkham, R.V., Sinclair, W.D., Thorpe, R.I., Duke, J.M.  
 481 (Eds.), *Mineral deposit modeling*. Mineral. Assoc. Can. Special Paper 40, 521-554.

482 Chamberlain, K.R., 1998. Medicine Bow orogeny: Timing of deformation and model of crustal  
 483 structure produced during continent-arc collision, ca. 1.78Ga, southeastern Wyoming.  
 484 *Rocky Mts. Geol.* 33, 259-277.

485 Chamberlain, K.R., Frost, C.D., Frost, B.R., 2003. Early Archean to Mesoproterozoic  
 486 evolution of the Wyoming Province: Archean origins to modern lithospheric architecture.  
 487 Can. J. Earth. Sci. 40, 1357-1374.

488 Dilles, J.H., 1987. Petrology of the Yerington Batholith, Nevada - evidence for evolution of  
 489 Porphyry copper ore fluids. Econ. Geol. 82, 1750-1789.

490 Doe, B.R., Tilling, R.I., Hedge, C.E., Klepper, M.R., 1968. Lead and strontium isotope studies  
 491 of the Boulder Batholith, southwestern Montana. Econ. Geol. 63, 884-906.

492 Downes, H., MacDonald, R., Upton, B.G.J., Cox, K.G., Bodinier, J.L., Mason, P.R.D., James,  
 493 D., Hill, P.G., Hearn, B.C., 2004. Ultramafic xenoliths from the Bearpaw Mountains,  
 494 Montana, USA: Evidence for multiple metasomatic events in the lithospheric mantle  
 495 beneath the Wyoming craton. J. Petrol. 45, 1631-1662.

496 Dueker, K., Yuan, H., Zurek, B., 2001. Thick Proterozoic lithosphere of the Rocky Mountains  
 497 region. GSA Today 11, 4-9.

498 Esperanca, S., Carlson, R.W., Shirey, S.B., 1988. Lower crustal evolution under central  
 499 Arizona - Sr, Nd and Pb isotopic and geochemical evidence from the mafic xenoliths of  
 500 Camp Creek. Earth Planet. Sci. Lett. 90, 26-40.

501 Farmer, G.L., DePaolo, D.J., 1983. Origin of Mesozoic and tertiary granite in the western  
 502 United-States and implications for pre-Mesozoic crustal structure.1. Nd and Sr isotopic  
 503 studies in the geocline of the northern Great-Basin. J. Geophys. Res. 88, 3379-3401.

504 Farmer, G.L., DePaolo, D.J., 1984. Origin of mesozoic and tertiary granite in the western  
 505 United-States and implications for pre-Mesozoic crustal structure.2. Nd and Sr isotopic  
 506 studies of unmineralized and Cu-mineralized and Mo-mineralized granite in the  
 507 Precambrian craton. J. Geophys. Res. 89, 141-160.

508 Foster, D.A., Mueller, P.A., Mogk, D.W., Wooden, J.L., Vogl, J.J., 2006. Proterozoic evolution  
 509 of the western margin of the Wyoming craton: implications for the tectonic and magmatic  
 510 evolution of the northern Rocky Mountains. Can. J. Earth Sci. 43, 1601-1619.

511 Frost, C.D., Frueh, B.L., Chamberlain, K.R., Frost, B.R., 2006a. Archean crustal growth by  
 512 lateral accretion of juvenile supracrustal belts in the south-central Wyoming Province. Can.  
 513 J. Earth Sci. 43, 1533-1555.

514 Frost, C.D., Frost, B.R., Kirkwood, R., Chamberlain, K.R., 2006b. The tonalite-trondhjemite-  
515 granodiorite (TTG) to granodiorite-granite (GG) transition in the late Archean plutonic rocks  
516 of the central Wyoming Province. *Can. J. Earth Sci.* 43, 1419-1444.

517 Galer, S.J.G., 1986. Chemical and isotopic studies of crust-mantle differentiation and the  
518 generation of mantle heterogeneity, Ph.D. Thesis, University of Cambridge, pp 220.

519 Griffin, W.L., O'Reilly, S.Y., Afonso, J.C., Begg, G.C., 2009. The composition and evolution of  
520 lithospheric mantle: a re-evaluation and its tectonic implications. *J. Petrol.* 50, 1185-1204.

521 Gunther, D., Audetat, A., Frischknecht, R., Heinrich, C.A., 1998. Quantitative analysis of  
522 major, minor and trace elements in fluid inclusions using laser ablation inductively coupled  
523 plasma mass spectrometry. *J. Anal. Atom. Spectrom.* 13, 263-270.

524 Halter, W.E., Pettke, T., Heinrich, C.A., 2002. The origin of Cu/Au ratios in porphyry-type ore  
525 deposits. *Science* 296, 1844-1846.

526 Halter, W., Heinrich, C.A., Pettke, T., 2005. Magma evolution and the formation of porphyry  
527 Cu-Au ore fluids: evidence from silicate and sulfide melt inclusions. *Mineral. Dep.* 39, 845-  
528 863.

529 Harry, D. L., Leeman, W.P. 1995. Partial melting of melt metasomatized subcontinental  
530 mantle and the magma source potential of the lower lithosphere. *J. Geophys. Res.* 100(B6),  
531 10255-10269.

532 Hart, W.K., Carlson, R.W., Shirey, S.B., 1997. Radiogenic Os in primitive basalts from the  
533 northwestern USA: Implications for petrogenesis. *Earth Planet. Sci. Lett.* 150, 103-116.

534 Hattori, K.H., Keith, J.D., 2001. Contribution of mafic melt to porphyry copper mineralization:  
535 evidence from Mount Pinatubo, Philippines, and Bingham Canyon, Utah, USA. *Mineral.*  
536 *Dep.* 36, 799-806.

537 Hawkesworth, C., Turner, S., Gallagher, K., Hunter, A., Bradshaw, T., Rogers, N., 1995. Calc-  
538 alkaline magmatism, lithospheric thinning and extension in the Basin and Range. *J.*  
539 *Geophys. Res.* 100(B6), 10271-10286.

540 Hildreth, W., Moorbath, S. 1988. Crustal contributions to arc magmatism in the Andes of  
541 central Chile. *Contrib. Mineral. Petrol.* 98, 455-489.

542 Hildreth, W., 1981. Gradients in silicic magma chambers - implications for lithospheric  
543 magmatism. *J. Geophys. Res.* 86, 153-192.

544 Holland, H.D. 2005. 100<sup>th</sup> anniversary special paper: Sedimentary mineral deposits and the  
545 evolution of earth's near-surface environments. *Econ. Geol.* 100, 1489-1509.

546 Hou, Z.Q., Cook, N.,J., 2009. Metallogensis of the Tibetan collisional orogen: A review and  
547 introduction to the special issue. *Ore Geol. Rev.* 36, 2-24.

548 Johnson, C.M., 1991. Large-scale crust formation and lithosphere modification beneath  
549 middle to late Cenozoic calderas and volcanic fields, western North-America. *J. Geophys.*  
550 *Res.* 96(B8), 13485-13507.

551 Johnson, C.M., Lipman, P.W., Czamanske, G.K., 1990. H, O, Sr, Nd, and Pb isotope  
552 geochemistry of the latir volcanic field and cogenetic intrusions, New-Mexico, and relations  
553 between evolution of a continental magmatic center and modifications of the lithosphere.  
554 *Contrib. Min. Petrol.* 104, 99-124.

555 Karlstrom, K.E., Whitmeyer, S.J., Dueker, K., Williams, M.L., Bowring, S.A., Levander, A.,  
556 Humphreys, E.D., Keller, G.R., the CD-ROM Working Group, 2004. Synthesis of results  
557 from the CD-ROM experiment: 4-D image of the lithosphere beneath the rocky mountains  
558 and implications for understanding the evolution of continental lithosphere. In Karlstrom,  
559 K.E., Keller, G.R. (Eds.), *The Rocky Mountain Region: An Evolving Lithosphere —*  
560 *Tectonics, Geochemistry, and Geophysics. Geophysical Monograph Series 154, 421 - 480.*  
561 *ISBN 0-87590-419-X*

562 Kempton, P.D., Fitton, J.G., Hawkesworth, C.J., Ormerod, D.S., 1991. Isotopic and trace-  
563 element constraints on the composition and evolution of the lithosphere beneath the  
564 southwestern United-States. *J. Geophys. Res.* 96(B8), 13713-13735.

565 Kessel, R., Schmidt, M.W., Ulmer, P., Pettke, T., 2005. Trace element signature of  
566 subduction-zone fluids, melts and supercritical liquids at 120-180 km depth. *Nature* 437,  
567 724-727.

568 Kleine, T., Munker, C., Mezger, K., Palme, H., 2002. Rapid accretion and early core formation  
569 on asteroids and the terrestrial planets from Hf-W chronometry. *Nature* 418, 952-955.

570 Klemm, L.M., Pettke, T., Heinrich, C.A., 2008. Fluid and source magma evolution of the  
 571 Questa porphyry Mo deposit, New Mexico, USA. *Mineral. Dep.* 43, 533-552.

572 Kramers, J.D., Tolstikhin, I.N., 1997. Two terrestrial lead isotope paradoxes, forward transport  
 573 modelling, core formation and the history of the continental crust. *Chem. Geol.* 139, 75-110.

574 Landtwing, M.R., 2004. Fluid evolution and ore mineral precipitation at the Bingham porphyry  
 575 Cu-Au-Mo deposit, Utah, deduced from cathodoluminescence imaging and LA-ICPMS  
 576 microanalysis of fluid inclusions. Unpublished PhD Thesis Nr. 15361, ETH Zurich, pp 260.

577 Landtwing, M.R., Pettke, T., Halter, W.E., Heinrich, C.A., Redmond, P.B., Einaudi, M.T.,  
 578 Kunze, K., 2005. Copper deposition during quartz dissolution by cooling magmatic-  
 579 hydrothermal fluids: The Bingham porphyry. *Earth Planet. Sci. Lett.* 235, 229-243.

580 Landtwing, M.R., Furrer, C., Redmond, P.B., Pettke, T., Guillong, M., Heinrich, C.A., 2010.  
 581 The Bingham Canyon porphyry Cu-Mo-Au deposit: III. Zoned copper - gold ore deposition  
 582 by magmatic vapor expansion. *Econ. Geol.* 105, 91-118.

583 Leeman, W.P., Harry, D.L., 1993. A binary source model for extension-related magmatism in  
 584 the Great-Basin, Western North-America. *Science* 262, 1550-1554.

585 Maughan, D.T., Keith, J.D., Christiansen, E.H., Pulsipher, T., Hattori, K., Evans, N.J., 2002.  
 586 Contributions from mafic alkaline magmas to the Bingham porphyry Cu-Au-Mo deposit,  
 587 Utah, USA. *Mineral. Dep.* 37, 14-37.

588 Mirnejad, H., Bell, K., 2008. Geochemistry of crustal xenoliths from the Hatcher Mesa  
 589 lamproite, Wyoming, USA: Insights into the composition of the deep crust and upper mantle  
 590 beneath the Wyoming craton. *Can. Mineral.* 46, 583-596.

591 Mueller, P.A., Frost, C.D., 2006. The Wyoming Province: a distinctive Archean craton in  
 592 Laurentian North America. *Can. J. Earth Sci.* 43, 1391-1397.

593 Mueller, P.A., Heatherington, A.L., Kelly, D.M., Wooden, J.L., Mogk, D.W., 2002.  
 594 Paleoproterozoic crust within the Great Falls tectonic zone: Implications for the assembly of  
 595 southern Laurentia. *Geology* 30, 127-130.

596 Muntener, O., Ulmer, P., 2006. Experimentally derived high-pressure cumulates from hydrous  
 597 arc magmas and consequences for the seismic velocity structure of lower arc crust.  
 598 *Geophys. Res. Lett.* 33, L21308.

599 Parry, W.T., Wilson, P.N., Moser, D., Heizler, M.T., 2001. U-Pb dating of zircon and Ar-40/Ar-  
600 39 dating of biotite at Bingham, Utah. *Econ. Geol.* 96, 1671-1683.

601 Pettke, T., 2008. Analytical protocols for element concentration and isotope ratio  
602 measurements in fluid inclusions by LA-(MC)-ICP-MS. In: *Laser ablation ICP-MS in the*  
603 *Earth Sciences: Current practices and outstanding issues* (Sylvester, P., ed). Mineral.  
604 Assoc. Can. Short Course Series 40, 189-218.

605 Pettke, T., Oberli, F., Audetat, A., Wiechert, U., Harris, C. R., Heinrich, C. A., 2008. Precise  
606 and accurate lead isotopic analysis of fast transient signals by laser-ablation MC-ICP-MS.  
607 *Geochim. Cosmochim. Acta* 72, A741.

608 Pilet, S., Baker, M.B., Stolper, E.M., 2008. Metasomatized lithosphere and the origin of  
609 alkaline lavas. *Science* 320, 916-919.

610 Presnell, R. D., 1997. Structural controls on the plutonism and metallogeny in the Wasatch  
611 and Oquirrh Mountains, Utah. In: John, D.A., Ballantyne, G.H. (eds) *Geology and ore*  
612 *deposits of the Oquirrh and Wasatch Mountains, Utah*. Guidebook Series of the Society of  
613 *Economic Geologists* 29, 69-90. ISBN 1-887483-29-2.

614 Qu, X.M., Hou, Z.Q., Zaw, K., Li, Y.G., 2007. Characteristics and genesis of Gangdese  
615 porphyry copper deposits in the southern Tibetan Plateau: Preliminary geochemical and  
616 geochronological results. *Ore Geol. Rev.* 31, 205-223.

617 Redmond, P.B., Einaudi, M.T., Inan, E.E., Landtwing, M.R., Heinrich, C.A., 2004. Copper  
618 deposition by fluid cooling in intrusion-centered systems: New insights from the Bingham  
619 porphyry ore deposit, Utah. *Geology* 32, 217-220.

620 Redmond, P.B., Einaudi, M.T., 2010. The Bingham Canyon porphyry Cu-Mo-Au deposit: I.  
621 Sequence of intrusions, vein formation and sulfide deposition. *Econ. Geol.* 105, 43-68.

622 Scambelluri, M., Pettke, T., van Roermund, H.L.M., 2008. Majoritic garnets monitor deep  
623 subduction fluid flow and mantle dynamics. *Geology* 36, 59-62.

624 Schoenberg, R., Kamber, B.S., Collerson, K.D., Eugster, O., 2002. New W-isotope evidence  
625 for rapid terrestrial accretion and very early core formation. *Geochim. Cosmochim. Acta* 66,  
626 3151-3160.

- Seo, J.H., Guillong, M., Heinrich, C.A., 2009. The role of sulfur in the formation of magmatic-hydrothermal copper-gold deposits. *Earth Planet. Sci. Lett.* 282, 323-328.
- Singer, D.A., Berger, V.I., Moring, B.C., 2005. *Porphyry Copper Deposits of the World: Database, Map, and Grade and Tonnage Models*. U.S. Geological Survey Open-File Report 2005-1060. <http://pubs.usgs.gov/of/2005/1060/>
- Singer, B.S., Jicha, B.R., Leeman, W.P., Rogers, N.W., Thirlwall, M.F., Ryan, J., Nicolaysen, K.E., 2007. Along-strike trace element and isotopic variation in Aleutian Island arc basalt: Subduction melts sediments and dehydrates serpentine. *J. Geophys. Res.* 112, B06206.
- Souders, A.K., Frost, C.D., 2006. In suspect terrane? Provenance of the late Archean Phantom Lake metamorphic suite, Sierra Madre, Wyoming. *Can. J. Earth Sci.* 43, 1557-1577.
- Stacey, J.S., Moore, W.J., Rubright, R.D., 1967. Precision measurement of lead isotope ratios - preliminary analyses from US Mine, Bingham Canyon, Utah. *Earth Planet. Sci. Lett.* 2, 489-499.
- Stacey, J.S., Zartman, R.E., Nkomo, I.T., 1968. A lead isotope study of galenas and selected feldspars from mining districts in Utah. *Econ. Geol.* 63, 796-814.
- Stein, H.J., Hannah, J.L., 1985. Movement and origin of ore fluids in Climax-type systems. *Geology* 13, 469-474.
- Waite, K.A., Keith, J.D., Christiansen, E.H., Whitney, J.A., Hattori, K., Tingey, D.G., Hook, C.J., 1997. Petrogenesis of the volcanic and intrusive rocks associated with the Bingham Canyon porphyry Cu-Au-Mo deposit, Utah. In: John, D.A., Ballantyne, G.H. (eds) *Geology and ore deposits of the Oquirrh and Wasatch Mountains, Utah*. Guidebook Series of the Society of Economic Geologists 29, 69-90. ISBN 1-887483-29-2.
- Williams-Jones, A.E., Heinrich, C.A., 2005. 100<sup>th</sup> Anniversary special paper: Vapor transport of metals and the formation of magmatic-hydrothermal ore deposits. *Econ. Geol.* 100, 1287-1312.
- Zartman, R.E., 1974. Lead isotopic provinces in cordillera of western United-States and their geologic significance. *Econ. Geol.* 69, 792-805.

## Figure Captions



Fig. 1: Sketch of SW Laurentia (W USA) identifying major crustal segments (modified from Karlstrom et al., 2004, Foster et al., 2006). Archean crustal blocks (grey) are delimited by Proterozoic accretionary tectonic zones. Segments to the south of the Cheyenne Belt (CB) are terranes accreted during assembly of Laurentia, and sutures represent early Proterozoic subduction zones. The dash-dotted line separates terranes accreted to the Laurentian crustal block in the Phanerozoic. Filled black circles denote Bingham (Bh), situated on the Uinta Axis, Butte (Bt), Henderson (H) in the Colorado Mineral Belt, Questa (Q) on the eastern rim of the Cenozoic Rio Grande Rift (omitted for clarity), and the northern SE Arizona (SEAZ) ore district. F-L SZ refers to the Farewell Mt. - Lester Mt. Suture Zone.

Fig. 2: (A) Polished drill core cut showing the temporal relationships between successive intrusions and veining events at Bingham (Landtwing, 2004). The Quartz Monzonite Porphyry (QMP) is veined by stockwork quartz sulphide veins (Cu-Au vein) and then intruded by the Quartz Latite Porphyry (QLP). Hair quartz veinlets (not visible macroscopically) penetrated the rock before late quartz-molybdenite veining (Mo-vein) occurred. (B) Thick section photograph showing fluid inclusions and molybdenite crystals (black, labelled MoS<sub>2</sub>) in a quartz crystal from a quartz-molybdenite vein. The blow-up (C) identifies 3 brine inclusions analyzed for Pb isotope ratios that lie on the same plane as the black molybdenite crystal in the top-right corner. Labels correspond to analysis numbers in Table 1.

Fig. 3:  $^{208}\text{Pb}/^{206}\text{Pb}$  and  $^{207}\text{Pb}/^{204}\text{Pb}$  results for individual fluid inclusions from Bingham. A uniform Pb isotopic composition characterizes the texturally distinct Cu-Au (full symbols) and Mo (empty symbols) ore stages. Dashed lines separate inclusions from different samples (labels shown at the top of the diagram), identical symbols identify inclusions from the same fluid inclusion assemblage. Error bars are two standard error measurement uncertainties (2 s.e.m.), some of them smaller than symbol size.

Fig. 4: Graph of  $^{207}\text{Pb}/^{206}\text{Pb}$  vs.  $^{208}\text{Pb}/^{206}\text{Pb}$  for Bingham Cu-Mo-Au and other Mo-rich magmatic-hydrothermal ore deposits from the eastern Rocky Mountains. Bingham feldspar and fluid data define a linear trend (black solid line), which extrapolates to the more radiogenic values of the Butte porphyry-type Cu-Mo deposit and associated

magmatic rocks and to values measured for present-day depleted mantle (dotted area; Kramers and Tolstikhin, 1997), indicating a mixing relationship. Note that the Pb compositions of the fluid inclusions are uniform and cluster tightly at the non-radiogenic end (top right corner) of the Bingham array. Data for melanephelinite and shoshonite samples (Maughan et al., 2002) show more enriched  $^{208}\text{Pb}$ , interpreted to reflect source heterogeneities. The white star represents a propylitically altered pre-mineralization monzonite sample (Last Chance Stock) from Bingham. Data for lower-temperature galena of distal vein deposits at Bingham (Stacey et al., 1967), data fields for the least radiogenic Miocene hornblende andesite samples from the Latir Volcanic Field associated with Questa (Johnson et al., 1990) and for porphyry-Cu-Mo deposits from the northern SE Arizona district (SEAZ; Bouse et al., 1999) are shown for comparison. Analytical uncertainties (2 s.e.m.) are smaller than symbol size.

Fig. 5: In-situ Pb isotope data for feldspar phenocrysts and xenocrysts. Plot (A) shows K-feldspar data variably affected by the presence of polyphase inclusions in the ablated sample volume. The dashed arrows indicate the shift from inclusion-poor to inclusion-rich parts of the analytical signal of an individual spot ablation. Overall, there is no clear trend in Pb isotope data since the one analysis devoid of inclusions lies in the central part of the mixing trend. Plot (B) reveals distinct Pb isotopic difference between K-feldspar and plagioclase, indicating that magma mixing is at least partially responsible for the variable Pb signatures of the samples. Inter-sample and intra-sample Pb isotope disequilibrium characterizes the magmatic rocks at Bingham, reflecting primary variability (i.e., magma mixing) and, for K-feldspar, partial equilibration during magmatic-hydrothermal overprinting. Analytical uncertainties are 2 s.e.m., often smaller than symbol size.

Fig. 6: Comparison of Pb isotope data for xenoliths from lower crust and lithospheric mantle of the US Archean to Proterozoic lithosphere with the Bingham fluid inclusion and feldspar results. Data for SCLM are metasomatized mantle xenoliths (Carlson and Irving, 1994; Carlson et al., 2004), data for lower crust are represented by granulitic xenoliths (Proterozoic: Esperanca et al., 1988; Kempton et al., 1990; Carlson et al., 2004; Wyoming Craton: Bolhar et al., 2007; Mirnejad and Bell, 2008), Bingham

galena data are from Stacey et al. (1967), and Aleutian arc lava data (Singer et al., 2007) represent modern subduction zone magmatism. MORB-source mantle is after Kramers and Tolstikhin (1997). (A) Uranogenic diagram, (b) thorogenic diagram. Note that the Bingham data cluster tightly near the metasomatized mantle xenoliths from the Great Falls Tectonic Zone (Carlson and Irving, 1994) while crustal xenoliths vary strongly and are generally less (Wyoming Craton) or much more (Proterozoic terrains) radiogenic.

Fig. 7: Sketch illustrating our favourite scenario with 3 events (marked by stars on horizontal time axis) and two stages (dashed arrows) required to explain the Pb isotopic signatures of Bingham ore fluids. Juvenile crust, formed in the late Archean (event 1), evolves in isolation (stage 1) until this crust is subducted northwards during assembly of Laurentia in the early Proterozoic. Subduction fluids are released and metasomatize the overlying depleted mantle (dotted region, event 2) that evolves in isolation (stage 2) until partial melting of this metasomatized subcontinental lithospheric mantle is triggered by mild extensional tectonics in the late Eocene (event 3) to generate Bingham magmatism. Note that Cenozoic subduction is far to the west. WC refers to the Wyoming craton, CC to continental crust, and Prot. SCLM to Proterozoic subcontinental lithospheric mantle.

Fig. 8: (A) Forward modelling of the uranogenic (A) and thorogenic (B) two-stage Pb isotope evolution (stage 1, thick lines; stage 2, thin lines) that reproduces the measured Pb isotope signatures of Bingham ore fluids (grey star at 38 Ma).  $\mu$  values denote  $^{238}\text{U}/^{204}\text{Pb}$ ,  $\kappa$  values  $^{232}\text{Th}/^{238}\text{U}$ . Ages are in million years (Ma) before present, the black stars marking the beginning of stages 1 and 2, respectively. The dashed MORB source mantle evolution line (Kramers and Tolstikhin, 1997) represents convecting, depleted mantle, the dotted line (A only) depicts primitive mantle. Data for other Mo-enriched porphyry deposits of the eastern Rocky Mountains, US (Area 1 of Zartman, 1997), are shown for comparison (Butte: Doe et al., 1968; Henderson: Stein and Hannah, 1985; hornblende andesite associated with Questa: Johnson et al., 1990; SEAZ: northern SE Arizona district Cu-Mo centres; Bouse et al., 1999). Variability in thorogenic Pb at relatively uniform  $^{206}\text{Pb}/^{204}\text{Pb}$  is interpreted to reflect heterogeneities

746 in Proterozoic subduction metasomatism as subduction devolatilization may generate  
747 large variations in Th/U of product fluids (Kessel et al., 2005).

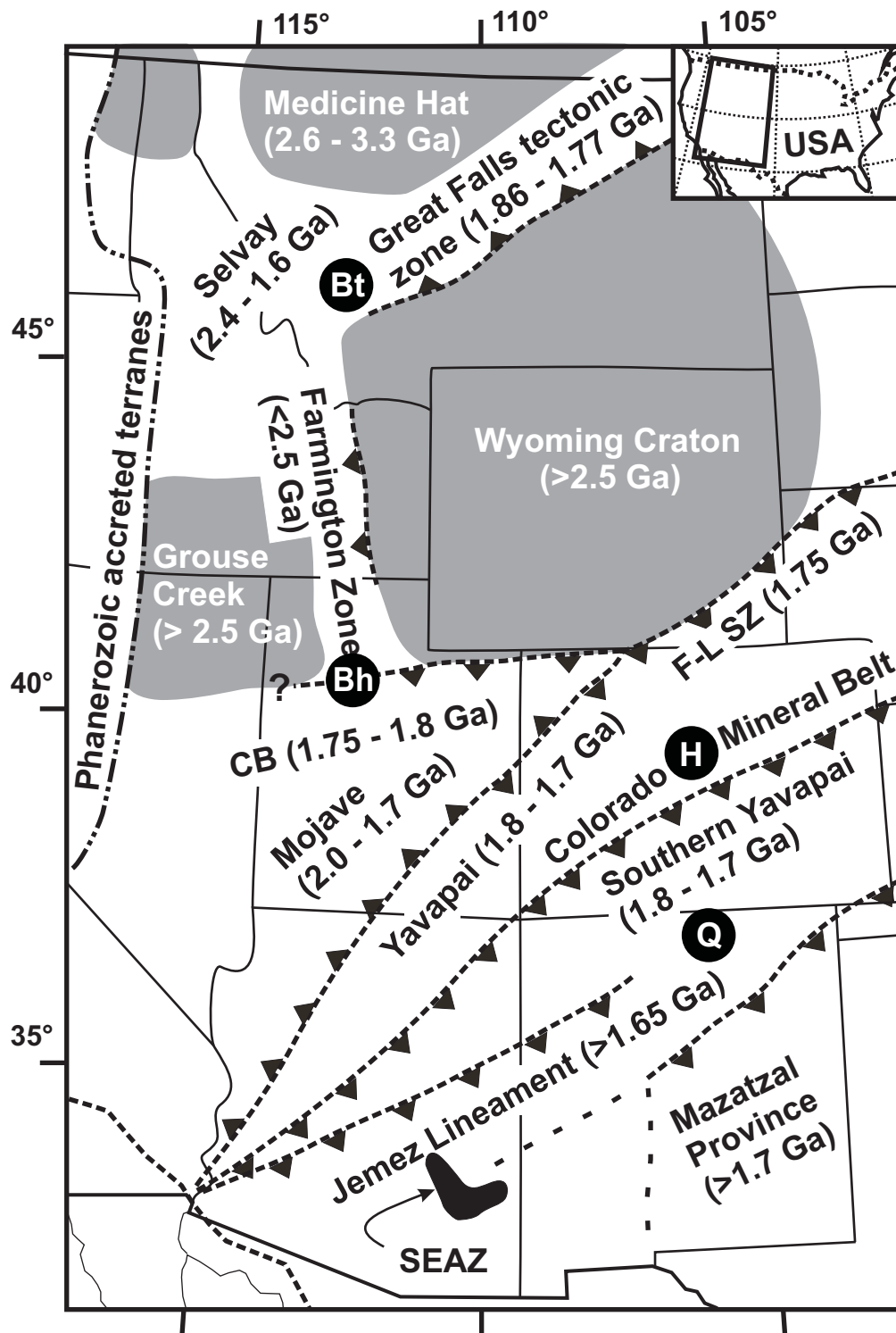


Figure 1

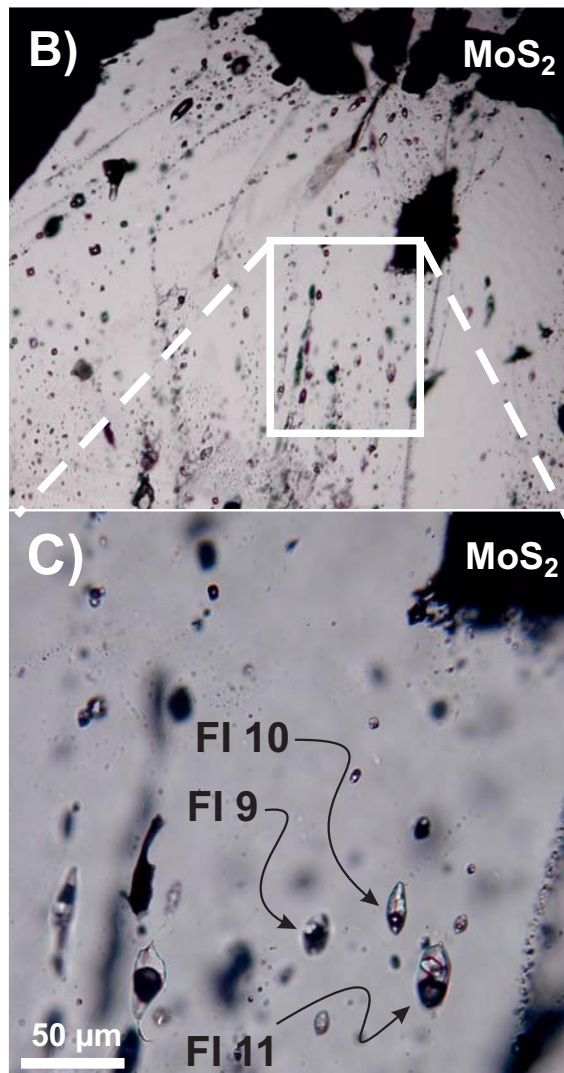
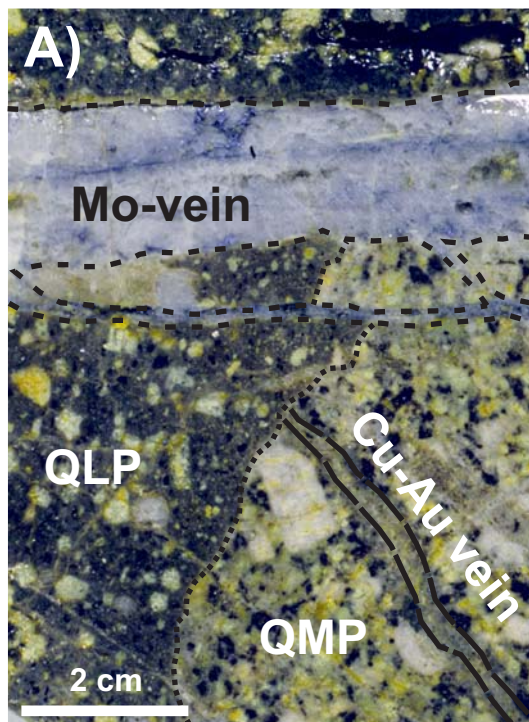


Figure 2

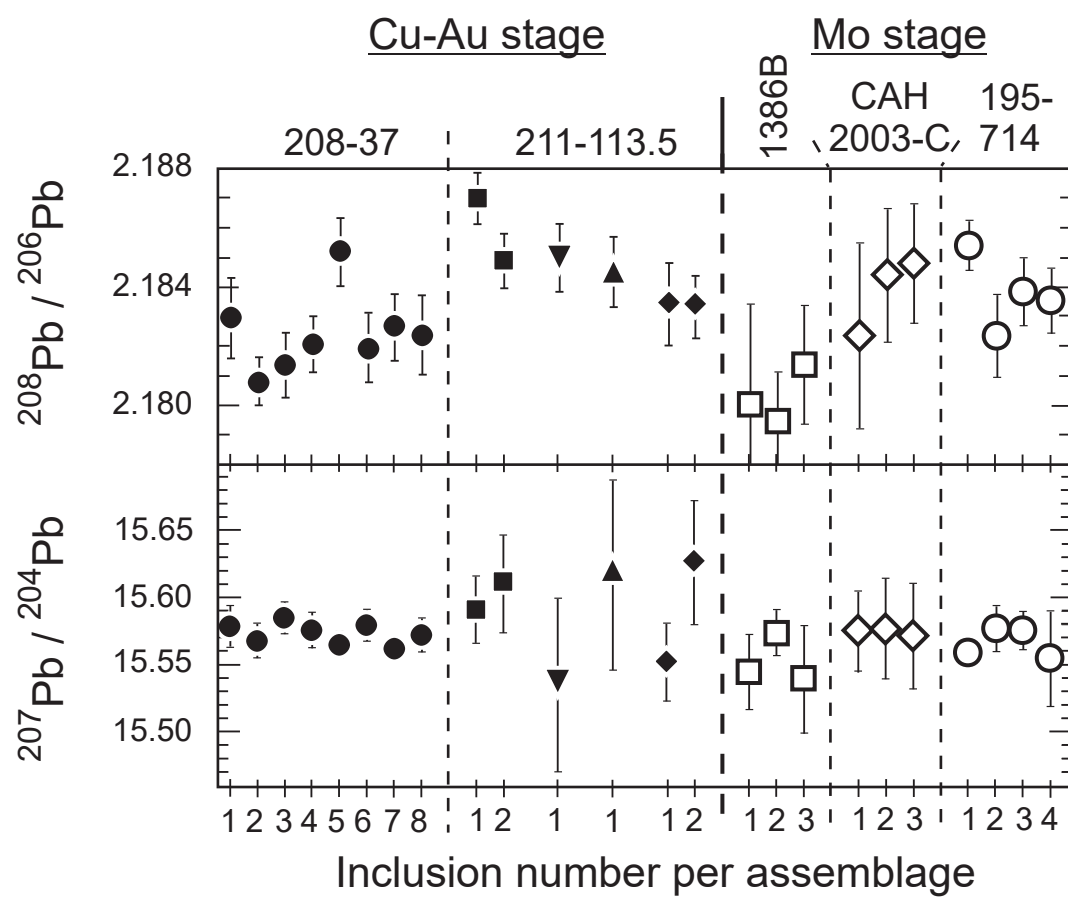


Figure 3

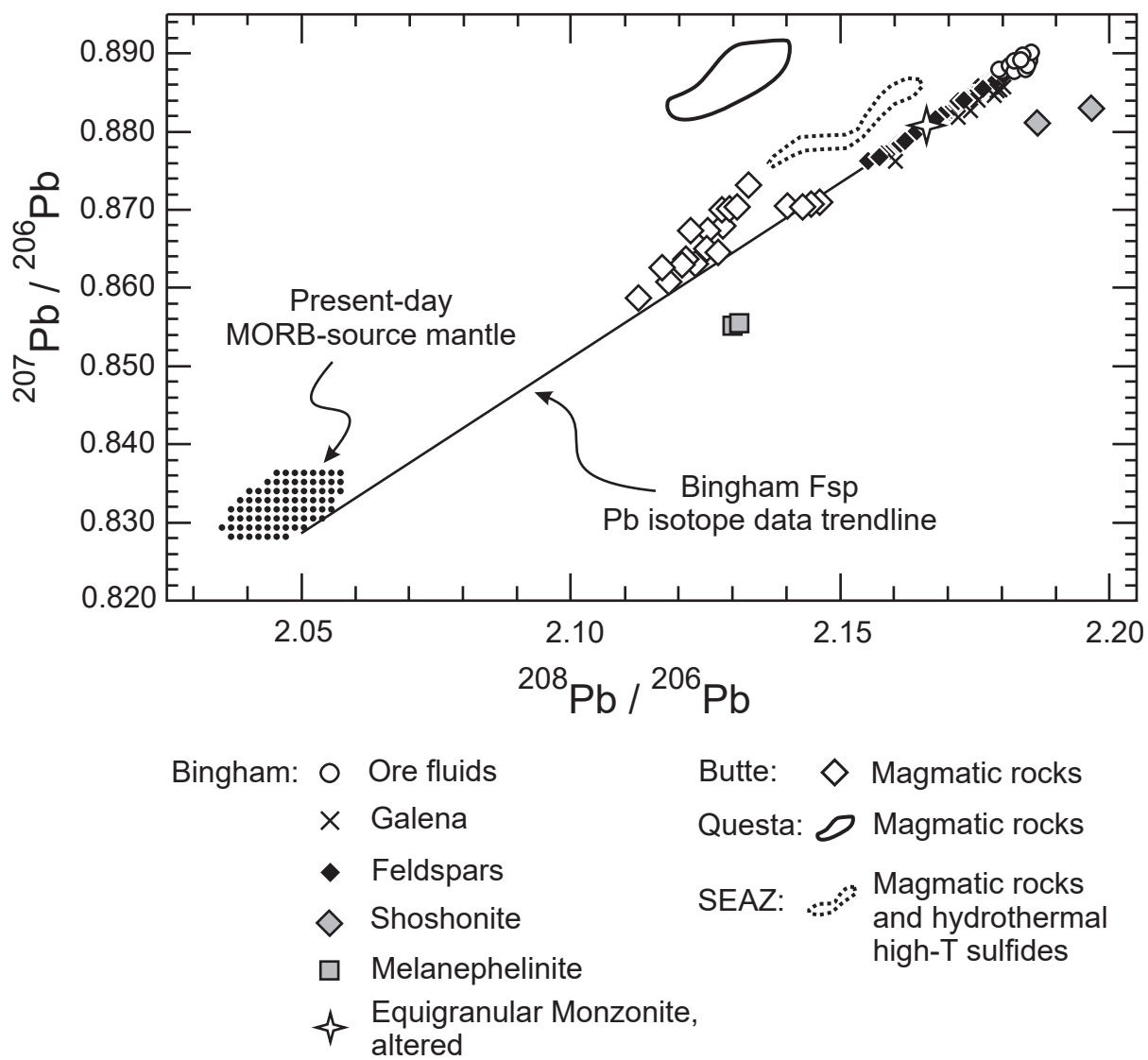


Figure 4



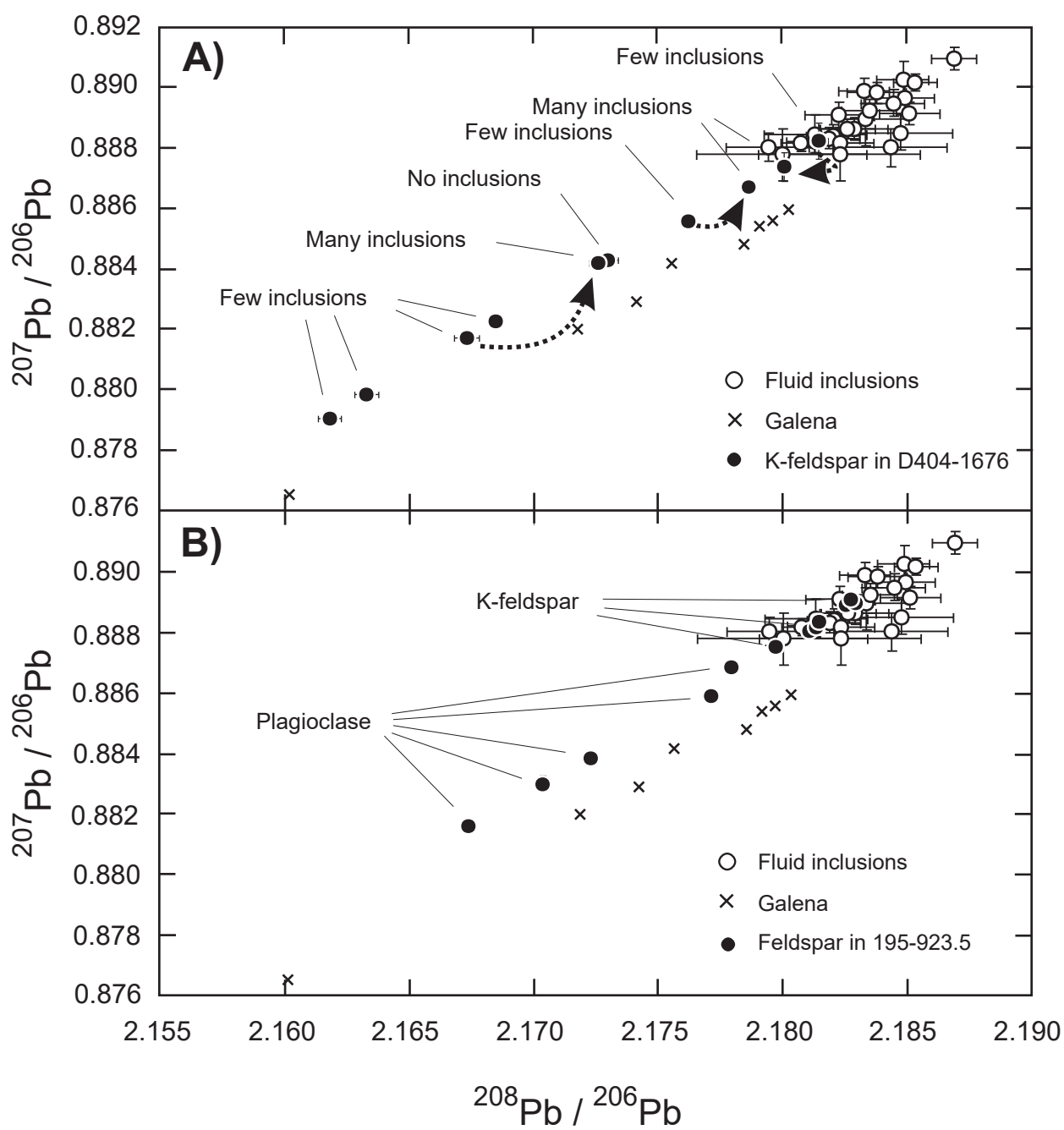


Figure 5

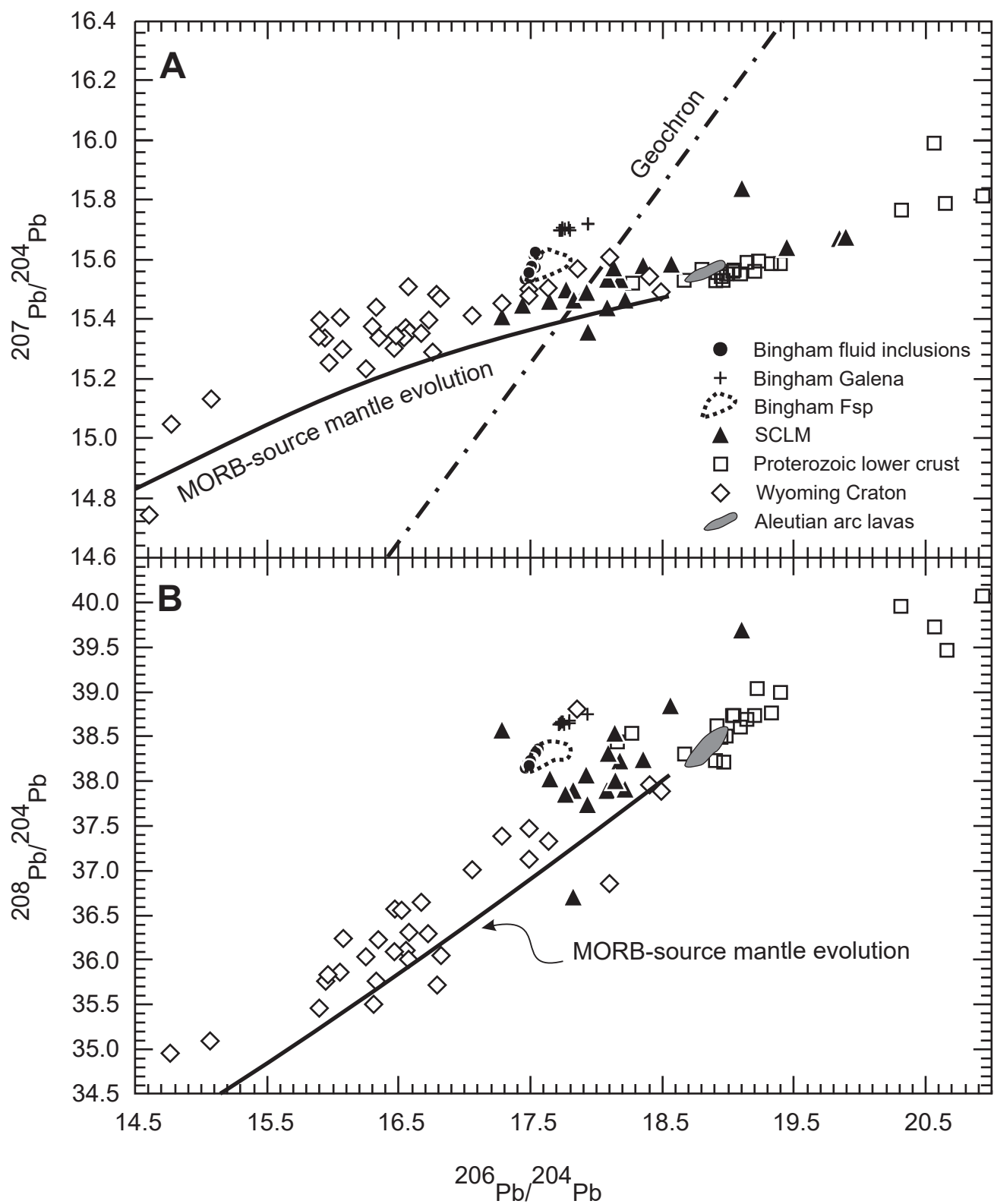


Figure 6

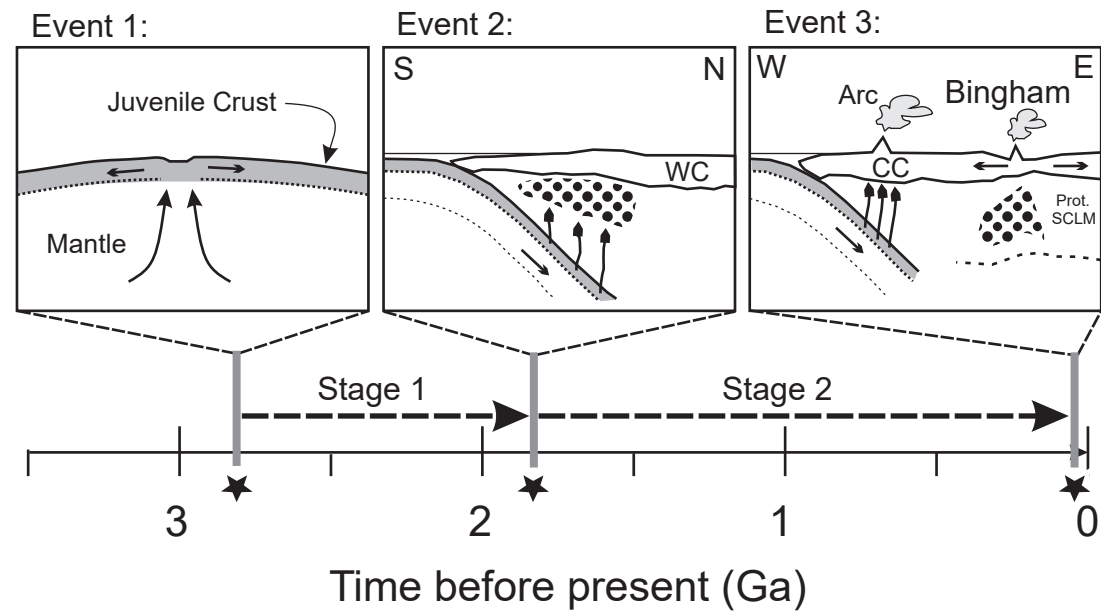


Figure 7

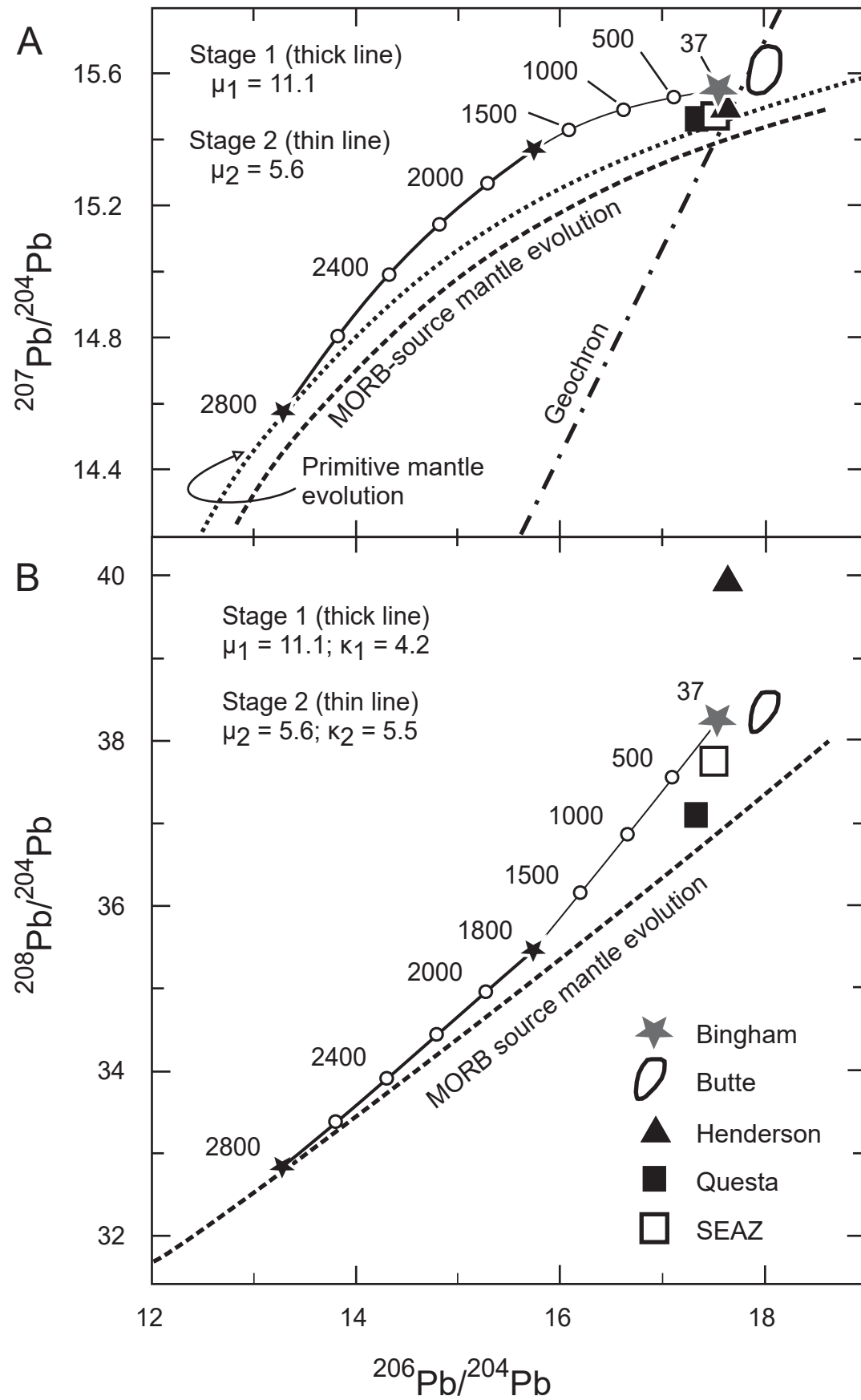


Figure 8

**Table 1: Pb isotope data of individual fluid inclusions (brines) from Cu-Au and Mo stage mineralizations at Bingham Canyon, USA**

Sample: FI number	<sup>208</sup> Pb/ <sup>206</sup> Pb	2 s.e.m. (meas)	<sup>207</sup> Pb/ <sup>206</sup> Pb	2 s.e.m. (meas)	<sup>206</sup> Pb/ <sup>204</sup> Pb	2 s.e.m. (meas)	<sup>207</sup> Pb/ <sup>204</sup> Pb	2 s.e.m. (meas)	<sup>208</sup> Pb/ <sup>204</sup> Pb	2 s.e.m. (meas)	Sample:	Mo (μg/g)	Cu (μg/g)	Au (μg/g)	Pb (μg/g)	U (μg/g)	Th (μg/g)
<b>Porphyry Cu-Au stage</b>																	
208-37: 1	2.1829	0.0014	0.88860	0.00039	17.518	0.016	15.578	0.015	38.281	0.043							
208-37: 2	2.1808	0.0008	0.88811	0.00029	17.529	0.014	15.568	0.013	38.232	0.037							
208-37: 3	2.1813	0.0011	0.88817	0.00036	17.539	0.013	15.586	0.012	38.278	0.033							
208-37: 4	2.1821	0.0011	0.88838	0.00036	17.526	0.014	15.575	0.013	38.259	0.037							
208-37: 5	2.1852	0.0012	0.88911	0.00036	17.505	0.012	15.565	0.010	38.264	0.027							
208-37: 6	2.1819	0.0012	0.88829	0.00036	17.530	0.012	15.578	0.012	38.266	0.033							
208-37: 7	2.1826	0.0011	0.88860	0.00033	17.509	0.008	15.562	0.008	38.225	0.024							
208-37: 8	2.1824	0.0013	0.88813	0.00039	17.523	0.012	15.573	0.013	38.269	0.037							
<b>Assemblage average</b>	<b>2.1824</b>		<b>0.88842</b>		<b>17.522</b>		<b>15.573</b>		<b>38.259</b>		<b>208-37 <sup>§</sup></b>	<b>86</b>	<b>11,400</b>	<b>0.077</b>	<b>3,610</b>	<b>n.m.</b>	<b>n.m.</b>
<b>Assemblage 2 s.d.</b>	<b>0.0026</b>		<b>0.00068</b>		<b>0.022</b>		<b>0.016</b>		<b>0.041</b>			<b>28</b>	<b>6,700</b>	<b>0.022</b>	<b>520</b>	<b>n.m.</b>	
211-113.5M: 19 <sup>§</sup>	2.1870	0.0009	0.89093	0.00036	17.519	0.029	15.591	0.025	38.293	0.065							
211-113.5M: 20 <sup>§</sup>	2.1849	0.0010	0.89023	0.00062	17.529	0.046	15.611	0.036	38.281	0.093							
211-113.5M: 21 <sup>§</sup>	2.1850	0.0012	0.88961	0.00070	17.456	0.071	15.534	0.065	38.142	0.156							
211-113.5M: 22 <sup>§</sup>	2.1845	0.0013	0.88945	0.00044	17.559	0.081	15.618	0.073	38.355	0.181							
<b>Sample average</b>	<b>2.1853</b>		<b>0.89006</b>		<b>17.516</b>		<b>15.588</b>		<b>38.268</b>		<b>211-19, trail G <sup>†</sup></b>	<b>42</b>	<b>26,100</b>	<b>n.m.</b>	<b>2,420</b>	<b>3</b>	<b>&lt;1</b>
<b>Sample 2 s.d.</b>	<b>0.0022</b>		<b>0.00135</b>		<b>0.087</b>		<b>0.076</b>		<b>0.180</b>			<b>9</b>	<b>8,300</b>	<b>n.m.</b>	<b>270</b>	<b>1</b>	
211-113.5N: 23 <sup>§</sup>	2.1834	0.0014	0.88893	0.00088	17.494	0.035	15.551	0.029	38.186	0.080							
211-113.5N: 24 <sup>§</sup>	2.1833	0.0010	0.88984	0.00042	17.536	0.052	15.624	0.047	38.314	0.111							
<b>Assemblage average</b>	<b>2.1834</b>		<b>0.88938</b>		<b>17.515</b>		<b>15.587</b>		<b>38.250</b>		<b>211-19, trail F <sup>†</sup></b>	<b>39</b>	<b>11,000</b>	<b>n.m.</b>	<b>3,100</b>	<b>5</b>	<b>n.m.</b>
<b>Assemblage 2 s.d.</b>	<b>0.0001</b>		<b>0.00128</b>		<b>0.060</b>		<b>0.103</b>		<b>0.181</b>			<b>22</b>	<b>7,500</b>	<b>n.m.</b>	<b>440</b>	<b>3</b>	
<b>Molybdenite stage</b>																	
1386B: 9	2.1800	0.0034	0.88773	0.00087	17.488	0.028	15.547	0.028	38.204	0.087							
1386B: 10	2.1795	0.0016	0.88798	0.00047	17.517	0.017	15.572	0.017	38.230	0.049							
1386B: 11	2.1814	0.0021	0.88843	0.00063	17.493	0.044	15.540	0.039	38.179	0.104							
<b>Assemblage average</b>	<b>2.1803</b>		<b>0.88805</b>		<b>17.500</b>		<b>15.553</b>		<b>38.204</b>		<b>JH2_BT2 <sup>*</sup></b>	<b>88</b>	<b>1,190</b>	<b>1.28</b>	<b>3,800</b>	<b>n.m.</b>	<b>n.m.</b>
<b>Assemblage 2 s.d.</b>	<b>0.0020</b>		<b>0.00070</b>		<b>0.032</b>		<b>0.034</b>		<b>0.051</b>			<b>87</b>	<b>950</b>	<b>1.03</b>	<b>970</b>		
CAH-2003-C: 12	2.1823	0.0032	0.88773	0.00085	17.543	0.030	15.574	0.030	38.307	0.077							
CAH-2003-C: 13	2.1844	0.0023	0.88799	0.00063	17.525	0.044	15.575	0.038	38.312	0.112							
CAH-2003-C: 14	2.1848	0.0021	0.88847	0.00057	17.535	0.046	15.571	0.039	38.313	0.102							
<b>Assemblage average</b>	<b>2.1838</b>		<b>0.88806</b>		<b>17.534</b>		<b>15.574</b>		<b>38.311</b>		<b>JH2-a7 <sup>*</sup></b>	<b>33</b>	<b>18,900</b>	<b>0.31</b>	<b>3,000</b>	<b>n.m.</b>	<b>n.m.</b>
<b>Assemblage 2 s.d.</b>	<b>0.0026</b>		<b>0.00074</b>		<b>0.019</b>		<b>0.004</b>		<b>0.007</b>			<b>32</b>	<b>7,500</b>	<b>0.12</b>	<b>230</b>		
195-714: 15	2.1854	0.0009	0.89012	0.00029	17.479	0.010	15.559	0.009	38.210	0.025							
195-714: 16	2.1823	0.0014	0.88906	0.00042	17.509	0.020	15.577	0.017	38.246	0.051							
195-714: 17	2.1838	0.0012	0.88979	0.00036	17.503	0.016	15.576	0.014	38.232	0.038							
195-714: 18	2.1835	0.0011	0.88921	0.00036	17.486	0.038	15.555	0.036	38.176	0.085							
<b>Assemblage average</b>	<b>2.1838</b>		<b>0.88955</b>		<b>17.494</b>		<b>15.567</b>		<b>38.216</b>								
<b>Assemblage 2 s.d.</b>	<b>0.0025</b>		<b>0.00099</b>		<b>0.029</b>		<b>0.023</b>		<b>0.061</b>								

**Notes:** Fluid inclusions were analyzed using a Nu Plasma 1700 ICP-MS, except for samples 211-113.5, analyzed using a Nu Plasma ICP-MS  
For inclusions, uncertainties are reported as twice the standard error of the mean of measurement (2 s.e.m.)  
For assemblage or sample averages, the uncertainty given is twice the standard deviation of the population (2 s.d.)  
Sample average denotes the average fluid composition of inclusions belonging to three fluid inclusion assemblages of that sample  
n.m. not measured  
<sup>§</sup> Data from this study. See Pettke (2008) for analytical details  
<sup>†</sup> Data from Landtwing (2004)  
<sup>\*</sup> Data from Seo et al. (2009)

**Table 2: Parameters explored in Monte Carlo simulations of Pb isotope evolution to reproduce the measured Bingham fluid Pb isotope data**

Simulation number	$\mu$ post-diff	T1 (Ga)	$^{206}\text{Pb}/^{204}\text{Pb}$ init (at T1)	$^{207}\text{Pb}/^{204}\text{Pb}$ init (at T1)	$^{208}\text{Pb}/^{204}\text{Pb}$ init (at T1)	$\mu 1$	$\kappa 1$	T2 (Ga)	$\mu 2$	$\kappa 2$
1	—	$2.8 \pm 0.1$	12.88 - 13.21	14.25 - 14.42	32.44 - 32.75	14.0 - 18.0	3.7 - 4.7	$1.8 \pm 0.1$	2.3 - 3.9	5.3 - 10.2
2	—	$3.2 \pm 0.1$	12.13 - 12.51	13.79 - 14.04	31.72 - 32.09	11.1 - 12.6	3.7 - 4.7	$1.8 \pm 0.1$	3.8 - 5.0	4.8 - 7.9
3	—	$2.8 \pm 0.1$	12.88 - 13.21	14.25 - 14.42	32.44 - 32.75	14.0 - 18.0	4.5 - 5.5	$1.8 \pm 0.1$	2.3 - 3.9	2.5 - 6.9
4	$8.0 \pm 0.2$	$2.8 \pm 0.1$	12.82 - 13.37	14.16 - 14.58	32.24 - 33.07	11.6 - 19.8	3.7 - 4.7	$1.8 \pm 0.1$	1.2 - 5.3	4.8 - 13.1
5	$8.5 \pm 0.2$	$2.8 \pm 0.1$	13.03 - 13.63	14.41 - 14.85	32.50 - 33.30	7.3 - 13.9	3.7 - 4.7	$1.8 \pm 0.1$	4.1 - 7.7	4.6 - 7.0
6	$9.0 \pm 0.2$	$2.8 \pm 0.1$	13.26 - 13.87	14.65 - 15.12	23.66 - 33.52	1.1 - 8.2	3.7 - 4.7	$1.8 \pm 0.1$	7.1 - 10.6	4.5 - 5.6

**Parameters used for modelling Pb evolution:**

The target Pb isotope signature for the simulations is that measured in Bingham fluid inclusions:

$$^{206}\text{Pb}/^{204}\text{Pb} = 17.515, ^{207}\text{Pb}/^{204}\text{Pb} = 15.573, ^{208}\text{Pb}/^{204}\text{Pb} = 38.252$$

Simulations 1-3 derive the starting Pb compositions for stage 1 from the model of Kramers and Tolstikhin(1997)

$\mu$ - and  $\kappa$ -values prior to core segregation are  $0.85 \pm 0.15$  and  $3.92 \pm 0.10$ , respectively

$\mu$  post-diff       $\mu$  value after Earth's core segregation at  $4.52 \pm 0.010$  Ga (Kleine et al., 2002, Schoenberg et al., 2002)

$\kappa$  post-diff       $\kappa$  value after Earth's core segregation, set at  $3.92 \pm 0.20$

T1                Start of stage 1 (in billion years before present)

Pb init           Range of initial Pb isotopic compositions at T1

$\mu 1$  and  $\kappa 1$     Range of  $\mu$  and  $\kappa$  values of stage 1

T2                Start of stage 2 set to 1.8 billion years before present

$\mu 2$  and  $\kappa 2$     Range of  $\mu$  and  $\kappa$  values of stage 2

# Supporting Online Material:

## The magma and metal source of giant porphyry-type ore deposits, based on lead isotope microanalysis of individual fluid inclusions

by Thomas Pettke, Felix Oberli and Christoph A. Heinrich

All LA-MC-ICP-MS Pb isotope analyses were performed at ETH Zurich using a GeoLas 200Q (Lambda Physik, Germany) laser system with computer-controlled sample stage connected to either a Nu Plasma 1700 or a Nu Plasma MC-ICP-MS instrument (Nu Instruments Ltd, Wrexham, UK). Table ES 1 summarizes the operating conditions for LA-ICP-MS analysis of Pb isotopes.

**Table ES 1:**  
**LA-MC-ICP-MS instrument and data acquisition parameters**

---

### 193 nm ArF Excimer laser Compex 110I

- Energy density on sample (J/cm <sup>2</sup> )	ca. 16, homogeneous across the ablation crater
- Pulse duration (ns)	ca. 15
- Repetition rate (Hz)	SRM (line scan): 6; SRM, FI and FSP (single spot): 10
- Shooting mode	1 $\mu\text{m s}^{-1}$ (line scan), single spot (SRM, FI, FSP)
- Pit sizes ( $\mu\text{m}$ )	SRM: 60 or 90; FI: 8 - 80; FSP: 80 - 120
- Ablation cell volume (cm <sup>3</sup> )	FI: 1, variable for SRM and FSP (1 - 16)
- Helium Cell gas flow (l min <sup>-1</sup> )	0.6

### Nu Plasma 1700 MC-ICP-MS \*

- Desolvator unit	DSN-100 desolvation nebulizer system
- Membrane Ar flow (l min <sup>-1</sup> )	2.9 - 3.1 (2.70 - 3.20)
- Auxiliary Ar flow (l min <sup>-1</sup> )	0.85 - 0.90 (0.75 - 1.00)
- Coolant Ar flow (l min <sup>-1</sup> )	13.0 (13.0 - 15.0)
- Power (W)	1,450 (1,100 - 1,550) fwd.; <2 reflected power
- Accelerating voltage (kV)	6
- Detector mode	Faraday, using 10 <sup>11</sup> $\Omega$ feedback resistors
- Interface pressure (mbar)	0.8 - 1.0
- Mass resolution (10% valley)	ca. 700

### Data acquisition parameters during transient signal analysis

- Acquisition mode	static, time-resolved
- Integration time	0.2 s
- Masses analyzed	200, 202, 203, 204, 205, 206, 207, 208

---

#### Notes:

Values reported in parentheses are the ranges explored during method development

SRM refers to SRM 610 glass from NIST

FI refers to fluid inclusions

FSP refers to plagioclase or K-feldspar phenocrysts

\* Operating conditions used at Nu Plasma MC-ICP-MS are similar to those reported here, with the exception of acceleration voltage (4kV) and mass resolution (ca. 400).

The MC-ICP-MS instrument was optimized daily for maximum sensitivity and perfect peak flatness and coincidence by admixing a desolvated aerosol generated from a 30 ppb Pb - 32 ppb Tl solution to the He flow from the LA chamber. Minor retuning was then performed by laser ablation on SRM 610 in line scan mode. The analyses were performed in static time-resolved mode, collecting the analytes simultaneously in Faraday cups calibrated daily for their preamplifier gains. For sample analysis, a background signal with laser off was acquired, then the Tl-solution was aspirated, and once the Tl signal was stable, LA was started, superimposing the sample signal on the Tl signal from the desolvating unit. Each ablation chamber loading was bracketed by 3 SRM 610 analyses to monitor instrument conditions.

Transient signal data reduction was done by revisiting the individually stored readings using modified Nu Instruments transient signal software, followed by off-line evaluation on Excel spreadsheets. After background correction of the analyte signals, Hg interference correction on raw mass 204 was effected based on the measured  $^{202}\text{Hg}$  beam and a  $^{204}\text{Hg}/^{202}\text{Hg}$  ratio of 4.32, adjusted to the fractionated state by use of an exponential mass bias coefficient derived from the measured  $^{205}\text{Tl}/^{203}\text{Tl}$  ratio and its common value of 2.3871 (Dunstan et al., 1980). Final  $^{208}\text{Pb}/^{206}\text{Pb}$  ratios (corrected for mass bias) do not correlate with  $^{202}\text{Hg}/\text{Pb}_{(\text{total})}$  ratios (not shown), thus demonstrating proper correction for Hg interference. Mass bias correction was exclusively done in within-run mode, using the Baxter et al. (2006) approach. Measurements of SRM 610 from NIST in line scan mode from >10 analytical sessions were used to define the mass bias, i.e., the instrument-specific  $\ln\text{Tl} - \ln\text{Pb}$  relationship for each Pb isotope ratio. For each sample analysis, the measured  $^{205}\text{Tl}/^{203}\text{Tl}$  isotope ratio was then used to correct for mass bias employing the  $\ln\text{Tl} - \ln\text{Pb}$  relationship established on the SRM 610 measurements. The sample Pb isotope ratios were obtained through individual processing of readouts from 0.2 s integration time slices. Data from each time-slice are individually treated for interference and mass bias correction, and the means calculated from these individual results then provide the isotope ratios of the sample.

Test measurements were performed on individual inclusions from synthetic fluid inclusions standards (prepared by A. Audetat, University of Bayreuth) containing ca. 5000  $\mu\text{g}$  SRM 981 Pb per g of NaCl-KCl solution of ca. 17 wt-% bulk salinity. Accurate Pb isotope data can be obtained on fluid inclusion assemblages with 2 SD uncertainties on inclusion-to-inclusion reproducibility of 0.06 % ( $^{208}\text{Pb}/^{206}\text{Pb}$  and  $^{207}\text{Pb}/^{206}\text{Pb}$  ratios) and 0.3% (Pb isotope ratios involving mass 204), respectively (Fig. S1). This is only possible, however, given controlled ablation of the entire fluid inclusion and integration of the entire transient signal (Pettke et al., 2008), in order to minimize bias originating from differences in signal decay parameters among the Faraday amplifiers used to record fast transient signals in multi-collector mode (more details to be published elsewhere). Acceptably reproducible results ( $\pm 1\text{‰}$  and  $5\text{‰}$ , respectively) were obtained for inclusions containing as little as 0.005 ng Pb using our setup with Faraday detectors.



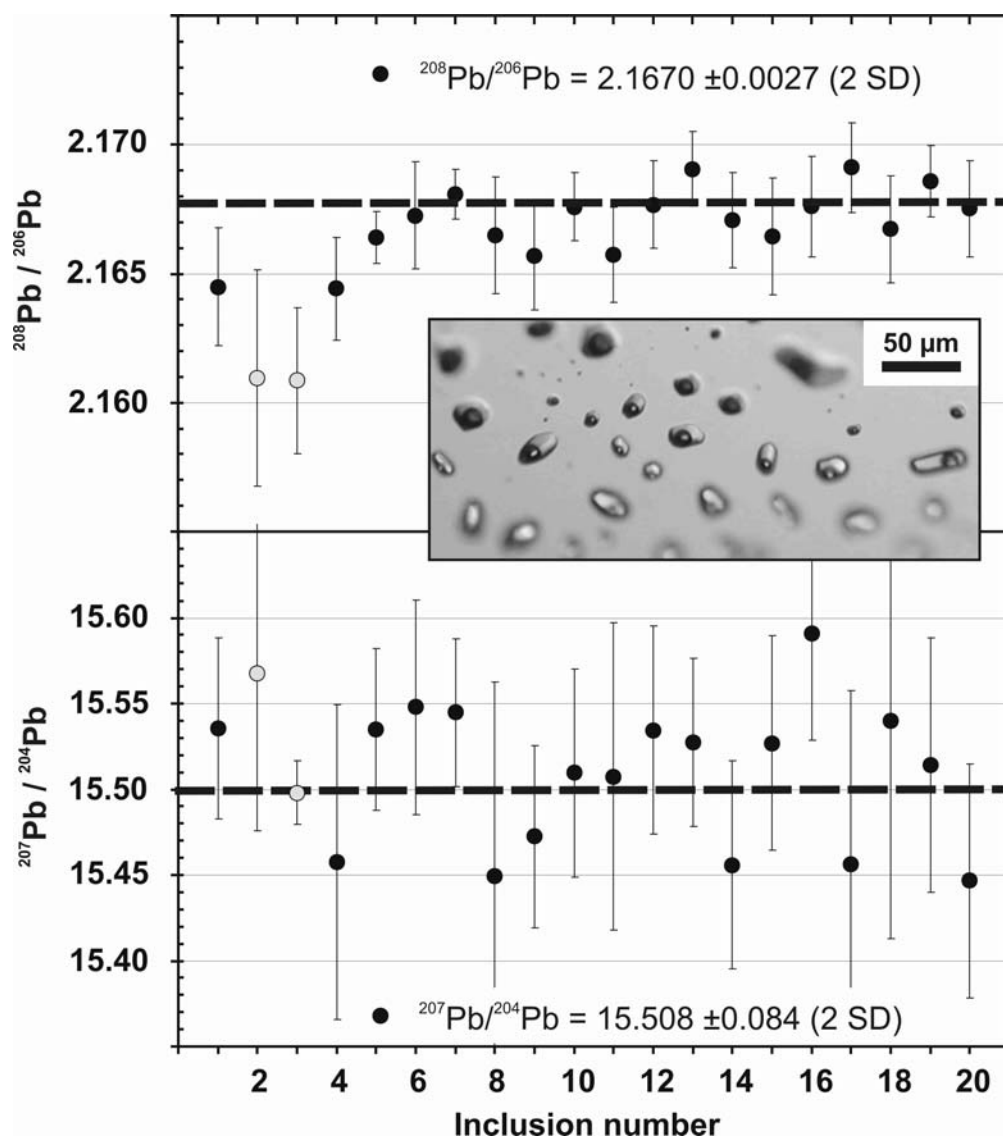


**Fig. S1:**

Thallium-normalized  $^{208}\text{Pb}/^{206}\text{Pb}$  and  $^{207}\text{Pb}/^{204}\text{Pb}$  ratios of individual synthetic fluid inclusions (inset) containing ca. 5000  $\mu\text{g}$  SRM 981 Pb per gram of Na-K-Cl fluid. Average measured isotopic ratios are reported with their 2 standard error uncertainty and reproduce the reference values of the standard (Baker et al., 2004) shown by the thick dashed lines. Analyses represented by grey symbols were excluded from the data set because fluid inclusion ablation was not well controlled.

## References

- Baxter D. C., Rodushkin I., Engstrom E., Malinovsky D., 2006. Revised exponential model for mass bias correction using an internal standard for isotope abundance ratio measurements by multi-collector inductively coupled plasma mass spectrometry. *J. Anal. Atom. Spectrom.* 21, 427-430.
- Dunstan L. P., Gramlich J. W., Barnes I. L., Purdy W. C., 1980. Absolute isotopic abundance and the atomic weight of a reference sample of thallium. *J. Res. National Bureau of Standards* 85, 1-10.
- Pettke T., Oberli F., Audetat A., Wiechert U., Harris C. R., Heinrich C. A., 2008. Precise and accurate lead isotopic analysis of fast transient signals by laser-ablation MC-ICP-MS. *Geochim. Cosmochim. Acta* 72, A741-A741.

**Table ES 2: Pb isotope data of feldspar (LA-MC-ICP-MS) and bulk rocks (solution MC-ICP-MS) from Bingham Canyon, and U-Th-Pb concentration data (LA-ICP-MS)**

Spot Number	Phase	Element conc. analysis Comments	Crater size (µm)	Pb (µg/g)	Th (µg/g)	U (µg/g)	Pb isot. analysis Comments	208Pb/206Pb	1 s.e.m. (meas)	207Pb/206Pb	1 s.e.m. (meas)	206Pb/204Pb	1 s.e.m. (meas)	207Pb/204Pb	1 s.e.m. (meas)	208Pb/204Pb	1 s.e.m. (meas)
<b>A57-5922.6 (Mine grids: -2403.21 E, +3329.77 N): Quartz Monzonite Porphyry</b>																	
1	Plag An23	clean	60	21.4	<0.005	<0.002	clean	2.17818	0.00010	0.88713	0.00009	17.587	0.016	15.599	0.014	38.309	0.035
2	Plag An24	clean	90	22.3	<0.002	<0.002	clean	2.17819	0.00013	0.88693	0.00011	17.540	0.017	15.561	0.016	38.223	0.039
3	Plag						clean	2.17992	0.00009	0.88779	0.00009	17.524	0.015	15.562	0.014	38.211	0.034
4	Plag An25	clean	90	22.9	21.6	<0.002	clean	2.17274	0.00016	0.88451	0.00013	17.574	0.022	15.545	0.020	38.183	0.050
5	Plag						clean	2.17399	0.00011	0.88451	0.00009	17.629	0.015	15.596	0.013	38.331	0.033
6	Plag An23	clean	60	22.6	21.5	<0.005	clean	2.17631	0.00010	0.88625	0.00016	17.593	0.034	15.591	0.030	38.261	0.075
7	Plag An24	clean	90	23.5	22.3	<0.002	clean	2.17716	0.00012	0.88646	0.00011	17.618	0.018	15.625	0.017	38.371	0.041
8	Plag						clean	2.16766	0.00013	0.88153	0.00011	17.662	0.020	15.574	0.018	38.288	0.044
<b>D195-567 (Mine grids: -1438.73 E, +447.51 N): Quartz Latite Porphyry</b>																	
1	AKF	clean	90	61.4	<0.002	<0.002	clean	2.17545	0.00011	0.88553	0.00008	17.626	0.015	15.611	0.013	38.342	0.033
2	AKF						clean	2.17344	0.00012	0.88448	0.00005	17.604	0.008	15.572	0.007	38.270	0.017
3	AKF						clean	2.17346	0.00009	0.88446	0.00006	17.601	0.011	15.568	0.010	38.257	0.024
4	AKF	clean	90	44.5	<0.004	<0.002	clean	2.18213	0.00009	0.88881	0.00005	17.517	0.007	15.573	0.006	38.239	0.015
5	AKF	clean	60	43.9	<0.002	<0.006	clean	2.18047	0.00010	0.88797	0.00007	17.544	0.012	15.587	0.011	38.264	0.027
6	Plag An23	clean, next to 120 µm pit	60	20.8	<0.007	<0.005	clean	2.18218	0.00010	0.88870	0.00008	17.516	0.015	15.563	0.014	38.216	0.034
6	Plag An24	clean	90	21.4	<0.002	0.002											
7	Plag An24	clean	60	22.5	<0.002	<0.005	clean	2.17392	0.00010	0.88451	0.00009	17.648	0.014	15.611	0.013	38.370	0.032
<b>D195-923.5 (Mine grids: -1438.73 E, +447.51 N): Quartz Latite Porphyry</b>																	
1	AKF						some inclusions	2.17970	0.00013	0.88755	0.00012	17.575	0.018	15.596	0.016	38.307	0.041
2	AKF						inclusions	2.18108	0.00009	0.88808	0.00005	17.530	0.007	15.570	0.006	38.237	0.015
3	AKF	clean	60	36.2	<0.008	<0.004	clean	2.18133	0.00009	0.88819	0.00007	17.579	0.013	15.615	0.012	38.352	0.029
4	AKF	many inclusions, next to pit	90	61.6	<0.004	0.004	many inclusions	2.18144	0.00010	0.88838	0.00005	17.533	0.006	15.578	0.005	38.255	0.013
4	AKF	many inclusions, next to pit	90	48.4	<0.002	0.010											
5	AKF	clean	60	39.4	<0.006	<0.008	few inclusions	2.18252	0.00010	0.88894	0.00005	17.510	0.008	15.570	0.007	38.226	0.018
6	AKF						many inclusions	2.18289	0.00017	0.88900	0.00011	17.526	0.015	15.585	0.014	38.246	0.033
7	AKF	clean, next to 120 µm pit	60	46.5	<0.004	<0.002	clean	2.18270	0.00009	0.88910	0.00005	17.530	0.006	15.586	0.006	38.270	0.014
8	Plag An24	clean	90	22.5	<0.002	<0.002	clean	2.17229	0.00010	0.88387	0.00007	17.663	0.014	15.613	0.013	38.374	0.032
9	Plag						clean	2.17038	0.00008	0.88302	0.00013	17.692	0.026	15.620	0.023	38.403	0.058
10	Plag An24	clean	60	21.2	<0.005	<0.005	clean	2.16742	0.00010	0.88163	0.00010	17.683	0.015	15.595	0.014	38.339	0.034
11	Plag An23	clean	60	22.0	<0.005	<0.002	clean	2.17792	0.00009	0.88687	0.00012	17.565	0.029	15.578	0.026	38.248	0.063
12	Plag						clean	2.17714	0.00014	0.88592	0.00011	17.606	0.018	15.601	0.017	38.335	0.041
<b>D195-1006 (Mine grids: -1438.73 E, +447.51 N): Biotite Porphyry</b>																	
1	Plag An24	clean, near pit	60	20.5	<0.005	<0.005	clean	2.17537	0.00011	0.88540	0.00010	17.585	0.016	15.567	0.015	38.267	0.037
2	Plag An23	clean	90	21.4	<0.002	0.002	clean	2.17521	0.00009	0.88516	0.00008	17.569	0.015	15.554	0.013	38.202	0.032
3	Plag						few inclusions	2.17621	0.00012	0.88577	0.00011	17.539	0.019	15.540	0.017	38.174	0.043
4	Plag						few inclusions	2.17869	0.00014	0.88657	0.00030	17.567	0.022	15.577	0.021	38.237	0.056
5	Plag An22	clean, between 2 pits	90	23.9	<0.002	<0.002	clean	2.17529	0.00009	0.88594	0.00029	17.542	0.032	15.548	0.029	38.197	0.069
12	Plag						clean	2.17327	0.00010	0.88453	0.00008	17.601	0.016	15.569	0.014	38.263	0.034
6	Plag						clean	2.17459	0.00010	0.88486	0.00008	17.606	0.015	15.576	0.014	38.303	0.035
7	Plag An23	clean, near pit	90	25.0	<0.002	<0.002	clean	2.17077	0.00011	0.88335	0.00010	17.621	0.017	15.568	0.015	38.264	0.037
8	Plag An24	clean	90	25.0	0.002	<0.005	clean	2.17135	0.00011	0.88364	0.00011	17.620	0.018	15.575	0.016	38.265	0.040
8	Plag An24						wider interval	2.17166	0.00009	0.88408	0.00010	17.596	0.014	15.561	0.012	38.217	0.031
9	Plag						clean	2.17540	0.00011	0.88509	0.00009	17.577	0.018	15.559	0.016	38.239	0.039
10	Plag						clean	2.17185	0.00011	0.88383	0.00009	17.583	0.017	15.542	0.015	38.201	0.037
11	Plag						clean	2.17421	0.00010	0.88479	0.00009	17.585	0.016	15.568	0.014	38.250	0.035
<b>D195-1181 (Mine grids: -1438.73 E, +447.51 N): Quartz Latite Porphyry</b>																	
1	AKF	near pits	60	44.1	<0.004	<0.004	clean	2.17460	0.00016	0.88469	0.00012	17.608	0.019	15.579	0.017	38.283	0.043
2	AKF						clean	2.17517	0.00018	0.88530	0.00014	17.620	0.030	15.601	0.027	38.353	0.070
3	AKF	clean	60	50.4	<0.004	<0.004	clean	2.17002	0.00013	0.88280	0.00009	17.659	0.016	15.590	0.014	38.323	0.034
4	AKF	clean, next to 120 µm pit	90	57.1	<0.004	<0.002	clean	2.17802	0.00010	0.88646	0.00005	17.591	0.008	15.595	0.007	38.317	0.018
5	AKF						clean	2.17080	0.00014	0.88303	0.00007	17.668	0.010	15.602	0.009	38.360	0.022
6	AKF	clean	90	51.8	<0.002	<0.002	clean	2.17255	0.00011	0.88375	0.00008	17.652	0.012	15.604	0.011	38.352	0.027
7	AKF	clean, next to 120 µm pit	60	39.3	<0.004	<0.004	clean	2.17289	0.00011	0.88393	0.00005	17.642	0.006	15.596	0.005	38.337	0.014

Table ES 2: continued

Spot number	Phase	Element conc. analysis Comments	crater size (µm)	Pb (µg g <sup>-1</sup> )	Th (µg g <sup>-1</sup> )	U (µg g <sup>-1</sup> )	Pb isot. analysis Comments	208Pb/206Pb final	1 s.e.m. (meas)	207Pb/206Pb final	1 s.e.m. (meas)	206Pb/204Pb (meas)	1 s.e.m. (meas)	207Pb/204Pb final	1 s.e.m. (meas)	208Pb/204Pb final	1 s.e.m. (meas)
<b>D404-1676 (Mine grids: -1652.83 E, -47.44 N): Quartz Monzonite Porphyry</b>																	
1	AKF	few small inclusions	60	35.2	<0.002	<0.002	inclusions	2.17624	0.00015	0.88561	0.00011	17.609	0.016	15.605	0.014	38.330	0.035
1							Inclusion signal	2.17868	0.00012	0.88674	0.00010	17.560	0.015	15.572	0.012	38.261	0.029
2	AKF	several small inclusions	60	30.4	0.014	0.008	inclusions	2.16851	0.00015	0.88227	0.00007	17.669	0.011	15.591	0.009	38.320	0.024
3	AKF	no inclusions	44	29.9	<0.006	0.008	clean	2.17300	0.00021	0.88431	0.00010	17.621	0.015	15.584	0.013	38.316	0.034
4	AKF						inclusions	2.18149	0.00019	0.88826	0.00029	17.524	0.066	15.565	0.058	38.229	0.147
4							Inclusion signal	2.18008	0.00015	0.88741	0.00024	17.523	0.058	15.552	0.054	38.206	0.122
5	AKF	many and big inclusions	60	30.5	<0.004	0.084 <sup>‡</sup>	inclusions	2.16330	0.00024	0.87984	0.00010	17.711	0.016	15.578	0.013	38.309	0.034
5							inclusions	2.16184	0.00023	0.87904	0.00009	17.765	0.013	15.618	0.012	38.410	0.032
6	AKF	many and big inclusions	60	51.7	<0.004	0.012	inclusions	2.16734	0.00026	0.88173	0.00012	17.680	0.019	15.591	0.017	38.312	0.041
6							Inclusion signal	2.17262	0.00018	0.88421	0.00008	17.617	0.130	15.579	0.110	38.279	0.280
<b>D504-594 (Mine grids: -5070.40 E +545.080 N): Quartz Latite Porphyry</b>																	
1	Plag An23	clean, next to 120 µm pit	60	35.2	<0.005	<0.005	clean	2.15896	0.00010	0.87783	0.00007	17.759	0.011	15.589	0.010	38.345	0.025
2	Plag						clean	2.16039	0.00008	0.87861	0.00006	17.739	0.010	15.586	0.009	38.326	0.023
3	AKF	full of inclusions, next to pit	90	79.9	0.094	0.023	full of inclusions	2.16090	0.00010	0.87868	0.00004	17.751	0.004	15.600	0.004	38.364	0.010
3	AKF	several inclusions	44	68.8	<0.012	<0.006											
4	Plag An24	clean, next to 120 µm pit	90	33.3	0.005	<0.002	clean	2.15741	0.00009	0.87729	0.00006	17.746	0.009	15.570	0.008	38.302	0.021
5	Plag						clean	2.15483	0.00009	0.87647	0.00009	17.798	0.016	15.598	0.014	38.355	0.035
6	Plag An22	clean, next to 80 µm pit	44	34.5	<0.007	<0.004	clean	2.15696	0.00010	0.87695	0.00011	17.741	0.020	15.560	0.017	38.262	0.044
<b>4890-2080 (surface sample, near Mine grids: -134 E, -1353 N): Quartz Latite Porphyry</b>																	
1	AKF	clean	120	53.1	<0.002	0.002	clean	2.18437	0.00009	0.88946	0.00005	17.495	0.008	15.561	0.007	38.213	0.017
2	AKF	clean	120	54.7	<0.002	0.002	clean	2.18399	0.00011	0.88930	0.00006	17.493	0.008	15.556	0.007	38.205	0.018
3	AKF	clean					clean	2.18426	0.00010	0.88940	0.00005	17.512	0.008	15.578	0.007	38.254	0.017
4	AKF	clean					clean	2.18417	0.00010	0.88944	0.00005	17.500	0.008	15.566	0.007	38.226	0.017
5		clean					clean	2.18497	0.00012	0.88967	0.00005	17.506	0.007	15.574	0.006	38.255	0.016
6		clean					clean	2.18437	0.00012	0.88930	0.00006	17.518	0.009	15.581	0.008	38.269	0.019
7		clean					clean	2.18440	0.00011	0.88933	0.00005	17.498	0.007	15.564	0.006	38.228	0.015
8		clean	120	58.2	<0.002	0.000	clean	2.18409	0.00018	0.88927	0.00007	17.489	0.011	15.554	0.009	38.217	0.024
9		clean	90	57.1	<0.004	<0.002	clean	2.18477	0.00012	0.88958	0.00005	17.491	0.008	15.557	0.007	38.213	0.017
<b>5090-980 (surface sample, near Mine grids: -134 E, -1353 N): Clast of Biotite Porphyry</b>																	
1	AKF	clean, near pit	60	48.7	<0.004	<0.008	clean	2.17386	0.00011	0.88441	0.00008	17.585	0.014	15.552	0.013	38.228	0.032
2	AKF	clean, near pit	60	38.2	<0.006	<0.004	a few inclusions	2.17786	0.00013	0.88636	0.00010	17.584	0.018	15.582	0.016	38.303	0.040
3	AKF	clean, near pit	60	42.2	<0.008	<0.004	clean	2.18074	0.00012	0.88757	0.00016	17.501	0.034	15.529	0.031	38.165	0.077
3	AKF						high-Pb peak	2.18137	0.00022	0.88854	0.00051	17.483	0.090	15.542	0.079	38.139	0.197
3	AKF						high-Pb peak	2.18159	0.00021	0.88886	0.00038	17.540	0.075	15.592	0.070	38.270	0.125
4	Plag An23	clean, near pit	90	23.2	<0.002	<0.002											
5	Plag An23	clean, near pit	90	23.2	<0.002	<0.002											
<b>Bulk rock <sup>†</sup></b>																	
	Melanepherinite	TICK 103, fresh						2.13029	0.00003	0.85502	0.00002	18.291	0.001	15.640	0.001	38.965	0.003
	Melanepherinite	TICK 120, fresh						2.13035	0.00005	0.85505	0.00001	18.287	0.001	15.636	0.001	38.957	0.002
	Shoshonite	TICK 116, fresh						2.18642	0.00003	0.87879	0.00001	17.827	0.001	15.666	0.001	38.978	0.002
	Shoshonite	TICK 117, fresh						2.19637	0.00002	0.88229	0.00001	17.748	0.000	15.659	0.000	38.981	0.001
	Equigran. Monz.	WR 8a, propyl. altered						2.16574	0.00003	0.88076	0.00001	17.697	0.000	15.587	0.000	38.328	0.001

**Notes:** For sample identifiers beginning with a letter followed by XXX-YYY, XXX is the drill core number and YYY is the depth (in ft) of core (Mine Grids are given in brackets)

For sample identifiers of the form XXXX-YYY, XXXX is the bench elevation and YYY is the distance along the bench (Mine Grids are given in brackets)

Lithologies are field determinations (Landtwing, 2004)

‡ Elevated U content due to ablation of inclusions

clean Indicates no visible inclusions

Uncertainties are reported as the one standard error of the mean of measurement (1 s.e.m.)

<value Element concentration below the limit of detection (3σ criterion)

† Coordinates for bulk rocks are not available, except Mine Grids for P 8a (-1150 E / -4850 N)